J. Fluid Mech. (1999), *vol.* 386, *pp.* 167–212. Printed in the United Kingdom

The surface layer for free-surface turbulent flows

By LIAN SHEN[1], XIANG ZHANG[1], DICK K. P. YUE[1]† AND GEORGE S. TRIANTAFYLLOU[2]

[1]Department of Ocean Engineering, Massachusetts Institute of Technology, Cambridge, MA 02139, USA
[2]The Levich Institute for Physio-Chemical Hydrodynamics, The City College of New York, New York, NY 10031, USA

(Received 11 July 1997 and in revised form 11 December 1998)

Direct numerical simulation (DNS) is used to examine low Froude number free-surface turbulence (FST) over a two-dimensional mean shear flow. The Navier–Stokes equations are solved using a finite-difference scheme with a grid resolution of 128^3. Twenty separate simulations are conducted to calculate the statistics of the flow. Based on the velocity deficit and the vertical extent of the shear of the mean flow, the Reynolds number is 1000 and the Froude number is 0.7. We identify conceptually and numerically the surface layer, which is a thin region adjacent to the free surface characterized by fast variations of the horizontal vorticity components. This surface layer is caused by the dynamic zero-stress boundary conditions at the free surface and lies inside a thicker blockage (or 'source') layer, which is due to the kinematic boundary condition at the free surface. The importance of the outer blockage layer is manifested mainly in the redistribution of the turbulence intensity, i.e. in the increase of the horizontal velocity fluctuations at the expense of the vertical velocity fluctuation. A prominent feature of FST is vortex connections to the free surface which occur inside the surface layer. It is found that as hairpin-shaped vortex structures approach the free surface, their 'head' part is dissipated quickly in the surface layer, while the two 'legs' connect almost perpendicularly to the free surface. Analysis of the evolution of surface-normal vorticity based on vortex surface-inclination angle shows that both dissipation and stretching decrease dramatically after connection. As a result, vortex structures connected to the free surface are persistent and decay slowly relative to non-connected vorticities. The effects of surface and blockage layers on the turbulence statistics of length scales, Reynolds-stress balance, and enstrophy dynamics are examined, which elucidate clearly the different turbulence mechanisms operating in the respective near-surface scales. Finally we investigate the effect of non-zero Froude number on the turbulence statistics. We show that the most significant effect of the presence of the free surface is a considerable reduction of the pressure–strain correlation at this surface, compared to that at a free-slip flat plate. This reduction is finite even for very low values of the Froude number.

1. Introduction

The physics of free-surface turbulence (FST) is essential to free-surface phenomena and processes such as the turbulent air–water interface, wind–wave interactions,

† Author to whom correspondence should be addressed.

post-breaking processes, and wakes. Recently, owing to the need to interpret the experimental data from remote sensing of ship wakes, FST became an active area of research. On a fundamental level, the study of FST may yield new insight into basic turbulence research. Therefore, there is a critical need to understand its basic mechanisms.

It should be pointed out that FST differs fundamentally from its counterpart, turbulence near a rigid wall. In general, a free surface affects turbulence by means of two mechanisms. First, in the absence of wind, the tangential stresses at the free surface should be zero, while near a rigid wall, velocity gradient is large, which makes turbulence production and dissipation significant there. Second, the free surface restricts motion in the normal direction only, while a no-slip condition at a rigid wall makes velocity components in all directions vanish.

Much of the work on turbulence in the past has been directed towards wall turbulence. Hunt & Graham (1978) analyse an interesting variation of the problem of turbulence interaction with a rigid wall, which resembles somewhat a stress-free boundary. They introduce a semi-infinite rigid wall which moves with the same speed as the mean velocity of grid turbulence. Near the wall, they identify two distinct boundary layers: an inner viscous layer and an outer source layer. Although the problem of Hunt & Graham (1978) is strictly not FST, it identifies some of the features characteristic of free-surface turbulence, and has inspired a number of other investigations in this area. Most of these investigations use the 'rigid lid' or 'free slip' approximation for the free surface, i.e. a flat surface with zero stresses but also zero normal velocity. This corresponds to the problem of free-surface turbulence in the limit of zero Froude number.

Perot & Moin (1995) use a novel idea to study the influence of a rigid wall on turbulence by considering separately two fictitious problems with 'simpler' boundary conditions. The first is a boundary which enforces no-slip but is otherwise permeable. This isolates and elucidates the viscous effects of a rigid wall. The second one they consider is in fact a flat free-slip boundary. This they use to isolate and investigate the kinematic effects that occur near the boundary. They find that it is the imbalance between splats and antisplats that leads to inter-component energy transfer near the surface. This imbalance is controlled by viscous processes and is found to be small for grid FST where there is no mean shear in the bulk flow underneath.

While Perot & Moin (1995) focus on the immediate effect of the presence of a free-slip boundary, Walker, Leighton & Garza-Rios (1996) study a similar grid FST case but consider the late time development after the imposition of the boundary. They identify two boundary layers where velocity and vorticity respectively are anisotropic and the thicknesses of these two layers are respectively the turbulence length scale and one-tenth of the turbulence length scale. Their analysis of the Reynolds-stress balance and enstrophy budget shows that the flow is fully three-dimensional up to the free surface.

Besides grid FST, another type studied in the past is that of open-channel flow. Early DNS work can be traced back to Lam & Banerjee (1988), Handler *et al.* (1991), Leighton, Swean & Handler (1991), and Swean *et al.* (1991), among others, who study the turbulent flow between a no-slip wall and a free-slip plate. Leighton *et al.* (1991) investigate the interaction of vorticity with the free surface and propose two models – the 'spin' model and the 'splat' model, which follow a description by Bradshaw & Koh (1981). Handler *et al.* (1993) study the Reynolds-stress balance and report that the dissipation rate exhibits a sharp drop near the surface. Handler *et al.* (1993) also study the variation of length scales and propose a 'pancake' model to explain

the increase of horizontal length scales and the decrease of vertical scales. These observations are reconfirmed and extended in the present study.

Vortex structures in open-channel flow is studied by Pan & Banerjee (1995). They identify large-scale persistent structures at the free surface, which include 'upwelling', 'downdraughts', and 'attached vortices'. They find that the attached vortices are particularly long-lived and tend to interact with each other unless destroyed by other upwellings. They conclude that turbulence structures near the free surface are quasi-two-dimensional.

Approximation of the free surface by a flat slip-free plate (zero Froude number limit) facilitates the numerical simulation and has been used extensively in the literature (Lam & Banerjee 1988; Handler *et al.* 1991; Leighton *et al.* 1991; Swean *et al.* 1991; Handler *et al.* 1993; Pan & Banerjee 1995; Perot & Moin 1995; and Walker *et al.* 1996, among others). Komori *et al.* (1993) use a non-zero Froude number which is however so small that there are no non-trivial differences from the zero Froude number case. Recently Borue, Orszag & Staroselsky (1995) studied the interaction of surface waves with turbulence in an open channel and find that the effect of non-zero Froude number on the turbulence statistics they examined is weak.

In the present paper we investigate numerically the development of turbulent shear flow under a free surface. The instability of this flow has been studied by Triantafyllou & Dimas (1989) and Dimas & Triantafyllou (1994). Aspects of this flow regarding the effects of underlying structures on surface roughness are described in Tsai (1998). In this study, we perform DNS for a large number of realizations of this free-surface turbulent shear flow to obtain reliable statistics. Through these simulations, we are able to: (i) identify the surface layer and the blockage layer and quantify the dynamics within these layers; (ii) understand the dynamics of surface vortex connections in FST and the underlying mechanisms for the persistence of such connected structures; and (iii) obtain the dominant effects of (even small) Froude number on the statistical characteristic of FST as compared to say turbulence under a free-slip wall. The elucidation of surface and blockage layers and their dynamics provides a coherent framework for understanding FST which clearly distinguishes it from turbulent flow near a no-slip wall, and, in a not insignificant way, from that near a free-slip wall.

This paper is organized as follows. In § 2, the concept of the surface layer and the blockage layer is introduced. In § 3, we outline the numerical scheme and provide specific quantitative results showing the presence of the surface and blockage layers. The spatial and temporal development of the surface layer during vortex surface connection events is studied in § 4. In § 5, we present the effects of the surface and blockage layers on the turbulence statistics with special emphasis on the turbulence length scales, Reynolds-stress balance and enstrophy dynamics. Finally, in § 6, we investigate the effect of Froude number on the FST statistics. For small (non-zero) Froude number, we find that the effects are relatively small with the exception of the pressure–strain correlations which show qualitative differences as a result of the free surface. We conclude in § 7 with a discussion and a summary.

2. The surface layer and the blockage layer

In this section we discuss the concept of the boundary layer that develops at a clean free surface. The frame of reference has axes x, y, z (also denoted as x_1, x_2, x_3 when tensor notation is used), where x and y are horizontal, z is vertical, positive upward, with the $z = 0$ plane coinciding with the undisturbed free surface.

The governing equations for the velocity components u_i (also denoted as u, v, or w)

are the Navier–Stokes equations

$$\frac{\partial u_i}{\partial t} + \frac{\partial (u_i u_j)}{\partial x_j} = -\frac{\partial p}{\partial x_i} + \frac{1}{Re}\frac{\partial^2 u_i}{\partial x_j \partial x_j}, \quad i = 1, 2, 3, \tag{2.1}$$

and the continuity equation

$$\frac{\partial u_i}{\partial x_i} = 0. \tag{2.2}$$

Here and hereafter, all variables are normalized by the characteristic (macro) length scale L and the characteristic velocity scale U of the flow. The dynamic pressure p is normalized by ρU^2, with ρ the fluid density. $Re \equiv UL/v$ is the Reynolds number, with v the kinematic viscosity.

We assume that the Froude number $Fr \equiv U/(gL)^{1/2}$ is small but not zero. Therefore, we use linearized free-surface boundary conditions at the position of undisturbed free surface $z = 0$.

(a) At the free surface, $z = 0$, the tangential stresses vanish:

$$\frac{1}{Re}\left(\frac{\partial u}{\partial z} + \frac{\partial w}{\partial x}\right) = 0 \quad \text{on} \quad z = 0, \tag{2.3}$$

$$\frac{1}{Re}\left(\frac{\partial v}{\partial z} + \frac{\partial w}{\partial y}\right) = 0 \quad \text{on} \quad z = 0. \tag{2.4}$$

(b) At the free surface, the normal stress vanishes which gives (neglecting surface tension)

$$p = \frac{h}{Fr^2} + \frac{2}{Re}\frac{\partial w}{\partial z} \quad \text{on} \quad z = 0, \tag{2.5}$$

where $h(x, y, t)$ is the free-surface elevation.

(c) Finally, the fact that the free surface moves as a material surface gives

$$\frac{\partial h}{\partial t} = w - u\frac{\partial h}{\partial x} - v\frac{\partial h}{\partial y} \quad \text{on} \quad z = h. \tag{2.6}$$

By linearization we obtain the kinematic boundary condition at the undisturbed free surface as

$$\frac{\partial h}{\partial t} = w - \frac{\partial}{\partial x}(uh) - \frac{\partial}{\partial y}(vh) \quad \text{on} \quad z = 0. \tag{2.7}$$

For $Re \gg 1$, the first term on the right-hand side of (2.5) is much larger than the second term, so that the requirement of vanishing normal stress is effectively an inviscid boundary condition. The effect of viscosity is thus manifest primarily through the vanishing of the tangential stresses (2.3) and (2.4). This can be seen most clearly in the horizontal components of the vorticity ω_i at the free surface. Using (2.3) and (2.4), we obtain

$$\omega_x = \frac{\partial w}{\partial y} - \frac{\partial v}{\partial z} = -2\frac{\partial v}{\partial z} = 2\frac{\partial w}{\partial y} \quad \text{on} \quad z = 0, \tag{2.8}$$

$$\omega_y = \frac{\partial u}{\partial z} - \frac{\partial w}{\partial x} = 2\frac{\partial u}{\partial z} = -2\frac{\partial w}{\partial x} \quad \text{on} \quad z = 0. \tag{2.9}$$

For small Froude numbers, h and w at the free surface are small, and it follows that ω_x and ω_y are small at $z = 0$. Finally, using the fact that vorticity is divergence free,

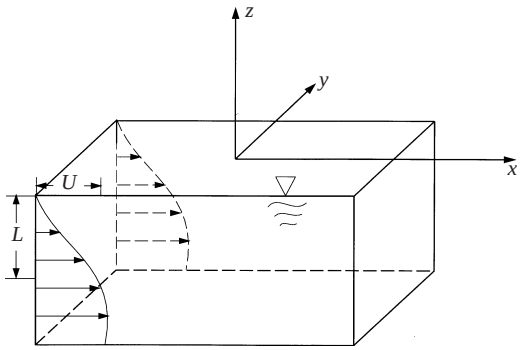

FIGURE 1. Definition sketch for shear-flow FST.

we obtain from (2.8) and (2.9) the boundary condition for ω_z on the free surface:

$$\frac{\partial \omega_z}{\partial z} = 0 \quad \text{on} \quad z = 0. \tag{2.10}$$

This simple analysis shows that, for flows with significant vorticity, there exists a *surface layer* inside which the values of ω_x, ω_y, and $\partial\omega_z/\partial z$ (but not ω_z itself) change from their 'outer' values to the much smaller values specified by (2.8), (2.9) and (2.10).

We note that the surface layer is thin for high Reynolds number. For laminar flow, a typical argument of balance between viscous and convection terms in the evolution equations for ω_x or ω_y shows that the thickness of the surface layer is proportional to the square root of the Reynolds number.

The surface layer, which is due to the viscous dynamic boundary conditions, is distinct from the so-called 'blockage' or 'source' layer, which is due to the kinematic boundary condition. The importance of the blockage layer is manifested mainly in the redistribution of the turbulence intensity, i.e. in the reduction of the vertical velocity fluctuations and the increase of the horizontal velocity fluctuations. From the continuity equation, the blockage layer has a thickness of order macroscale L.

The surface layer is unique to free-surface viscous flows, while the blockage layer obtains in principle for any flows with a boundary constraining the normal motion, for example, rigid wall flows and free-surface potential flows.

3. Numerical confirmation of the surface layer and the blockage layer

To elucidate the behaviour and to obtain quantitative properties of the surface layer, we perform direct numerical simulations of the incompressible Navier–Stokes equations for a turbulent shear flow evolving under a free surface.

3.1. *Problem definition*

We consider a three-dimensional incompressible turbulent flow in the presence of a free surface. As shown in figure 1, the turbulent flow has a mean velocity $\overline{u}(z,t)$ in the x-direction with the initial profile

$$\overline{u}(z, t = 0) = 1 - 0.9988\,\mathrm{sech}^2(0.88137z), \tag{3.1}$$

which is half of the mean velocity profile measured in the wake of a NACA 0003 hydrofoil in unbounded fluid (Mattingly & Criminale 1972). Here and hereafter, the initial mean shear flow depth L and velocity deficit U are used to normalize all the variables. Note that (3.1) is Galilean transformed with U as in the simulations.

The Orr–Sommerfeld stability analysis of the velocity profile (3.1) has been performed by Triantafyllou & Dimas (1989) and a detailed study on the nonlinear evolution of the instability is reported by Dimas & Triantafyllou (1994). Unlike open-channel flow, the turbulence in this sheared FST is generated solely from the mean shear in the bulk flow and is especially relevant to applications in naval hydrodynamics, such as ship wakes, and geophysical flows.

The motions of the flow are described by the Navier–Stokes equations (2.1) and the continuity equation (2.2), with the linearized free-surface boundary conditions (2.3), (2.4), (2.5), and (2.7).

At the bottom $z = -D$, we impose free-slip conditions:

$$\frac{\partial u}{\partial z} = \frac{\partial v}{\partial z} = 0, \tag{3.2}$$

$$w = 0, \tag{3.3}$$

$$\frac{\partial p}{\partial z} = 0. \tag{3.4}$$

Thus there is no turbulence production at the bottom and turbulence energy is extracted solely from the mean shear in the bulk flow. Finally we impose periodic boundary conditions in both horizontal directions.

3.2. *Numerical scheme*

The primitive-variable form of Navier–Stokes equations (2.1) and continuity equation (2.2) are solved numerically as an initial-boundary-value problem. The numerical method we use traces back to the marker and cell (MAC) method developed by Harlow & Welch (1965). We first use a projection method, which couples the continuity equation with the Navier–Stokes equations, to obtain a Poisson equation with a divergence correction for the pressure. The Poisson equation for the pressure is solved at each timestep. The simulation is then advanced explicitly to the next step. More specifically, knowing u_i^n, $i = 1, 2, 3$, at the current timestep, the time-discrete form of (2.1) is

$$\frac{u_i^{n+1} - u_i^n}{\Delta t} + \frac{\partial (u_i u_j)^n}{\partial x_j} = -\frac{\partial p^n}{\partial x_i} + \frac{1}{Re}\frac{\partial^2 u_i^n}{\partial x_j \partial x_j}. \tag{3.5}$$

Taking the divergence of (3.5) on both sides and invoking the continuity equation at the next step:

$$\frac{\partial u_i^{n+1}}{\partial x_i} = 0, \tag{3.6}$$

we obtain the following Poisson equation for the pressure p^n:

$$\frac{\partial^2 p^n}{\partial x_i \partial x_i} = \frac{1}{\Delta t}\frac{\partial u_i^n}{\partial x_i} + \frac{\partial}{\partial x_i}\left(-\frac{\partial (u_i u_j)^n}{\partial x_j} + \frac{1}{Re}\frac{\partial^2 u_i^n}{\partial x_j \partial x_j}\right). \tag{3.7}$$

This Poisson equation is solved subject to Dirichlet condition (2.5) at the free surface, Neumann condition (3.4) at the bottom, and periodic conditions in the horizontal directions. After the pressure p^n is obtained, velocity components are advanced explicitly in time using (3.5). In this study we use a second-order Runge–Kutta scheme for the time integration.

For space discretization, we use sixth-order finite-differences in the horizontal directions and second-order finite-difference in the vertical direction. To ensure mass conservation to machine accuracy, a staggered-grid system is employed in the vertical

direction wherein u, v, and p are assigned at regular grid positions while w is assigned at the positions with a vertical shift of half a grid spacing. In addition, mass conservation also requires that the horizontal operator $\partial^2 p/\partial x^2$ (similar for $\partial^2 p/\partial y^2$) be approximated by

$$\left.\frac{\partial^2 p}{\partial x^2}\right|_i = \frac{1}{3600\Delta x^2}(p_{i-6} - 18_{i-5} + 171p_{i-4} - 810p_{i-3} + 1935p_{i-2} + 828p_{i-1} - 4214p_i + 828p_{i+1} + 1935p_{i+2} - 810p_{i+3} + 171p_{i+4} - 18p_{i+5} + p_{i+6}) + O(\Delta x^6), \quad (3.8)$$

instead of the conventional form

$$\left.\frac{\partial^2 p}{\partial x^2}\right|_i = \frac{1}{180\Delta x^2}(2p_{i-3} - 27p_{i-2} + 270p_{i-1} - 490p_i + 270p_{i+1} - 27p_{i+2} + 2p_{i+3}) + O(\Delta x^6). \quad (3.9)$$

The argument is similar to Kwak, Reynolds & Ferziger's (1975) fourth-order case and will not be repeated here.

It should also be pointed out that the horizontal convection terms in the Navier–Stokes equations need a special energy-conservative scheme to avoid nonlinear instability (e.g. Kwak *et al.* 1975). Take the term $\partial(uv)/\partial x$, for example:

$$\begin{aligned}\left.\frac{\partial(uv)}{\partial x}\right|_i = {} & \frac{3}{8\Delta x}(u_{i+1}v_{i+1} - u_{i-1}v_{i-1} + u_i(v_{i+1} - v_{i-1}) + v_i(u_{i+1} - u_{i-1})) \\ & - \frac{3}{40\Delta x}(u_{i+2}v_{i+2} - u_{i-2}v_{i-2} + u_i(v_{i+2} - v_{i-2}) + v_i(u_{i+2} - u_{i-2})) \\ & - \frac{1}{120\Delta x}(u_{i+3}v_{i+3} - u_{i-3}v_{i-3} + u_i(v_{i+3} - v_{i-3}) + v_i(u_{i+3} - u_{i-3})) \\ & + O(\Delta x^6). \end{aligned} \quad (3.10)$$

It can be shown that in the absence of viscous terms and time-differencing errors, this scheme conserves energy to machine accuracy. A similar proof to this can again be found in Kwak *et al.* (1975).

Among the free-surface boundary conditions (2.3)–(2.7), the tangential dynamic conditions (2.3) and (2.4) are used in computing z-derivatives in (2.1); the normal free-surface dynamic condition (2.5) is used in the boundary condition for (3.7); and the kinematic free-surface condition (2.7) is used to update the free-surface elevation h in time.

3.3. *Computational parameters*

In this study, the Reynolds number $Re = UL/\nu$ is 1000 and the Froude number $Fr = U/(gL)^{1/2}$ is 0.7. If the velocity scale is based on the turbulence fluctuation instead, which we choose to be order of one tenth of U, the Reynolds number $Re_q \simeq 100$ and the Froude number $Fr_q \simeq 0.07$. The computational domain size is $10.472 \times 10.472 \times 4$ and we use a 128^3 grid. The horizontal domain size 10.472 corresponds to the minimum wavenumber 0.6, which is close to the most unstable mode for the mean shear profile (3.1) (Triantafyllou & Dimas 1989). The simulation is carried out from $t = 0$ to 90, with time step $\Delta t = 0.005$.

A rough estimate based on the theory of isotropic homogeneous turbulence (Tennekes & Lumley 1972) gives the (dimensionless) Kolmogorov scale:

$$\eta \sim \epsilon^{-1/4} Re^{-3/4} \simeq 0.04. \quad (3.11)$$

Here ϵ is the (dimensionless) dissipation rate for turbulence kinetic energy and is found to be $O(0.0005)$ in our numerical results (figure 20). The grid size in the horizontal directions is

$$\Delta_x = \Delta_y = \frac{10.472}{128} \simeq 0.08; \tag{3.12}$$

and the grid size in the vertical direction is

$$\Delta_z = \frac{4}{128} \simeq 0.03. \tag{3.13}$$

Thus the grid size is of the same order as the Kolmogorov scale.

To ensure that the dynamically significant scales are resolved, we also carry out a high-resolution simulation using a 256^3 grid, with a time step $\Delta t = 0.00125$, as well as a low-resolution simulation using a 64^3 grid. Comparison among the different resolutions of the 64^3 grid, 128^3 grid, and 256^3 grid shows that the difference between the 128^3 grid and 256^3 grid is small (cf. figure 4 for profiles of the mean flow velocity and the turbulence intensity).

The initial turbulence field in our simulation is implemented by the superposition of divergence-free random velocity noise upon the mean flow (3.1). Initially this random velocity noise is made to vanish at the free surface and the surface elevation is zero. As time goes on, energy is extracted from the mean shear flow to turbulence as the turbulent flow develops. From this point of view, the initial perturbations serve only as 'seeds' for the turbulence. This is in contrast with the cases of purely decaying turbulence, where the initial turbulence field needs to be constructed carefully, usually to match the experimental measurements.

To obtain convergent results for statistics, we perform repeated simulations using different seeds for the initial random field. Our experience shows that the variances become sufficiently small beyond about 20 simulations. Unless otherwise stated, all the results we present are ensemble averaged over (at least) 20 DNS realizations.

For later reference, we define the statistical average over the horizontal plane, where the turbulent flow is statistically homogeneous. For any variable $f(x, y, z, t)$, $\overline{f}(z, t)$ stands for the average over the horizontal plane; $f'(x, y, z, t) \equiv f - \overline{f}$ denotes the instantaneous fluctuation; and $f^{rms}(z, t) \equiv (\overline{f^2})^{1/2}$ its root-mean-square value.

3.4. *Overview of the flow field*

In this subsection, we give an overview of the time evolution of the shear flow. As pointed out earlier, turbulence is initially absent at the free surface and the surface is calm at $t = 0$. Supplied by the shear flow underneath, turbulence develops at the free surface as time evolves.

Figure 2 plots the time evolution of free-surface turbulence kinetic energy $q_0^2 \equiv (\overline{u'^2} + \overline{v'^2} + \overline{w'^2})|_{z=0}$, the fluctuation of free-surface elevation h'^{rms}, and their standard deviations. Initially, both the free-surface elevation and the turbulence intensity at the surface are zero. As free-surface turbulence develops, the flow reaches a quasi-steady state after about $t = 40$. At this quasi-steady state, the velocity fluctuation at the free surface q_0 is $O(0.1)$, which makes the Reynolds number based on turbulence intensity $Re_q \equiv q_0 L/\nu \simeq 100$ and the Froude number $Fr_q \equiv q_0/(gL)^{1/2} \simeq 0.07$. The fluctuation of the surface elevation h'^{rms} is about 0.005. Figure 2 shows that the free-surface elevation h'^{rms} normalized by Fr^2 is comparable to the free-surface turbulence kinetic energy $q_0^2/2$. This is indicative of the fact that some of the kinetic energy is transformed to potential energy in the surface fluctuations. Figure 2 also shows that

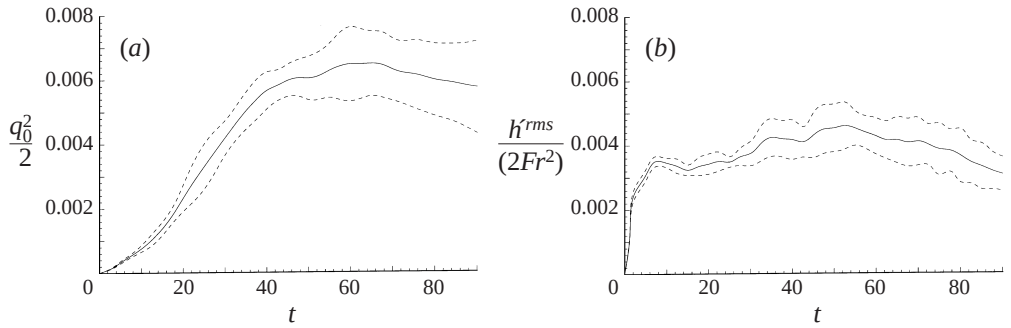

FIGURE 2. Evolution of (*a*) ———, free-surface turbulence kinetic energy $q_0^2/2$; – – – –, $q_0^2/2 \pm \sigma$; and (*b*) ———, fluctuation of free-surface elevation $h'^{rms}/(2F_r^2)$; – – – –, $h'^{rms}/(2F_r^2) \pm \sigma$. Here σ is the corresponding standard deviation.

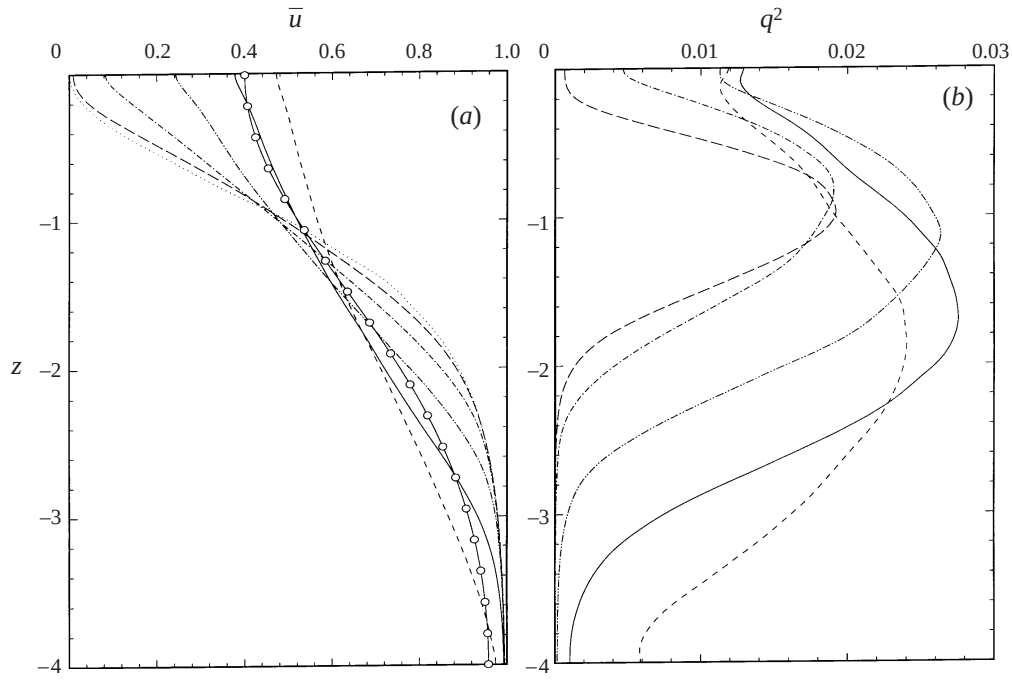

FIGURE 3. Evolution of (*a*) mean shear flow profile $\overline{u}(z,t)$; and (*b*) turbulence intensity profile $q^2(z,t)$. · · · · · · ·, $t = 0$; — —, $t = 5$; – · – · –, $t = 20$; —··—··—, $t = 40$; ———, $t = 60$; – – – –, $t = 80$. In (*a*) —○— is the mean flow profile for a laminar shear flow at $t = 60$. The laminar flow has the same initial profile (3.1) but Reynolds number $Re = UL/\nu$=100.

at later time ($t > 75$), dissipation exceeds the supply from below and the free-surface turbulence decays.

We plot in figure 3 the evolution of the mean shear flow profile $\overline{u}(z,t)$ and turbulence intensity profile $q^2(z,t) = \overline{u'^2} + \overline{v'^2} + \overline{w'^2}$. Owing to diffusion, the mean shear flattens as time increases. As expected, the diffusion due to turbulence transport is much larger than would be expected due to laminar diffusion. For a laminar shear flow with the same initial profile (3.1), we find that an equivalent Reynolds number to obtain a similar evolution of the mean velocity deficit is given by $Re = UL/\nu \approx 100$. This is

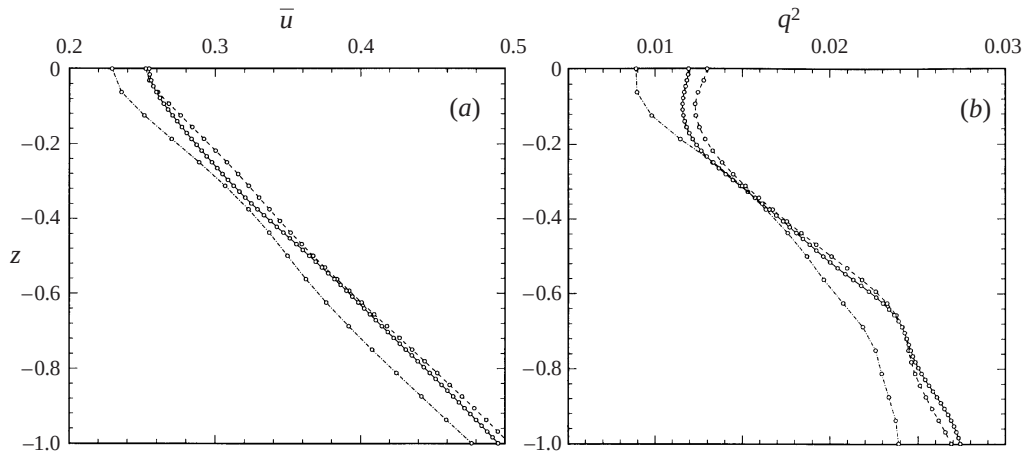

FIGURE 4. Comparison of (*a*) mean velocity $\overline{u}$ and (*b*) turbulence intensity q^2 at $t = 40$ for different DNS resolutions: – · – · –, 64^3 grid; – – – –, 128^3 grid; and ———, 256^3 grid.

shown in figure 3(*a*) which plots the comparison between the mean flow profiles for turbulent flow ($Re = 1000$) and laminar flow ($Re = 100$) at $t = 60$.

To show the convergence of the DNS, we plot in figure 4 the comparison between the results using the 64^3, 128^3, and 256^3 grids. The difference between the 128^3 and 256^3 resolution results is small, which indicates that the 128^3 grid is sufficient for solving the problem.

In this study we focus on the quasi-steady state when the turbulence production from the mean shear is balanced by the turbulence dissipation at the near-surface region. Hereafter, only the results from $t = 40$ to 75 are presented.

3.5. *Identification of the surface layer and the blockage layer*

The existence of the surface layer and the blockage layer is manifest in our DNS results of shear-flow FST. Figure 5 shows these two layers clearly. Figure 5(*a*) plots the vertical variation of $\omega_x'^{rms}$, $\omega_y'^{rms}$, $\omega_z'^{rms}$, and $(\partial\omega_z/\partial z)'^{rms}$, which give a clear indication of the surface layer which has a thickness of $O(0.1)$. Figure 5(*b*) plots the vertical profiles of the fluctuation velocity components $u_i'^{rms}$, which show distinctly the blockage layer of thickness $O(0.5)$ (the macroscale is $O(1)$).

The surface layer is also evident in the profile of the mean shear $\partial\overline{u}/\partial z$. Averaging the stress-free dynamics boundary condition (2.3) over the (x, y)-plane yields

$$\frac{\partial \overline{u}}{\partial z} = 0 \quad \text{on} \quad z = 0. \tag{3.14}$$

It can be anticipated that $\partial\overline{u}/\partial z$ (but not $\overline{u}$ itself) drops sharply over the surface layer, which is shown in figure 6.

As mentioned earlier, a free surface affects the underlying turbulent flow by means of two mechanisms: first, the dynamic boundary conditions require that the tangential stresses at the surface vanish; second, the kinematic boundary condition constrains the motion normal to the surface. The surface layer is where the dynamic boundary conditions are felt and the blockage layer is where the kinematic boundary condition is felt. Since the surface layer and the blockage layer are caused by different mechanisms at the free surface, the roles of the these two layers in the FST are distinct from each other. In § 5, we investigate the effects of each layer on the turbulence statistics

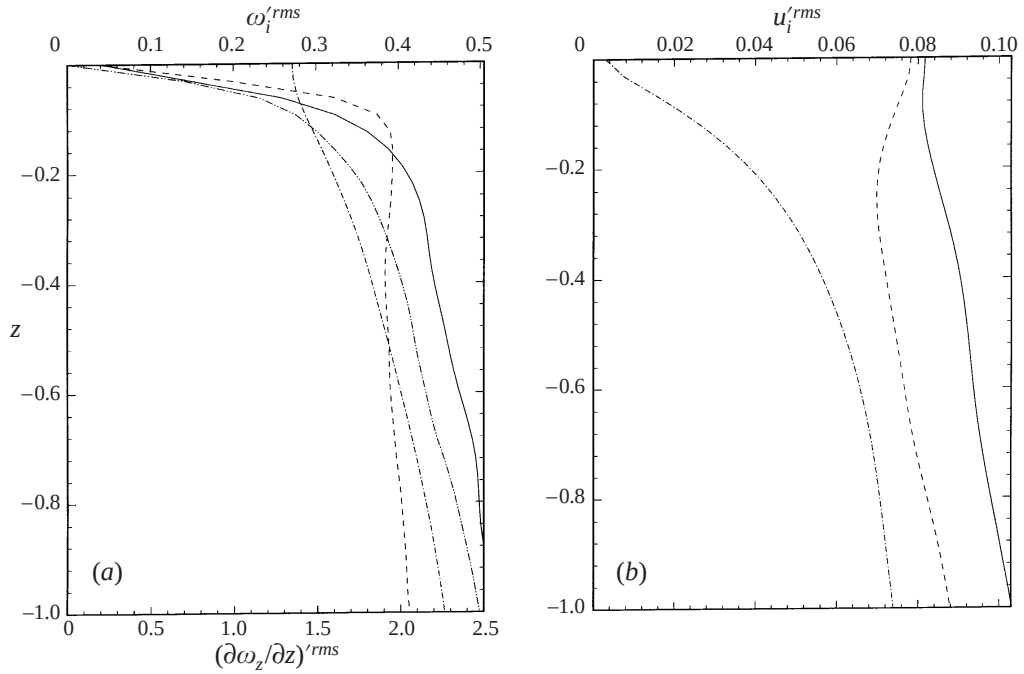

FIGURE 5. Existence of surface layer and blockage layer. (*a*) Surface layer: ———, $\omega_x'^{rms}$; – – – –, $\omega_y'^{rms}$; – · – · –, $\omega_z'^{rms}$; — · · — · · —, $(\partial\omega_z/\partial z)'^{rms}$; and (*b*) blockage layer: ———, u'^{rms}; – – – –, v'^{rms}; – · – · –, w'^{rms}. Results at $t = 60$ are plotted.

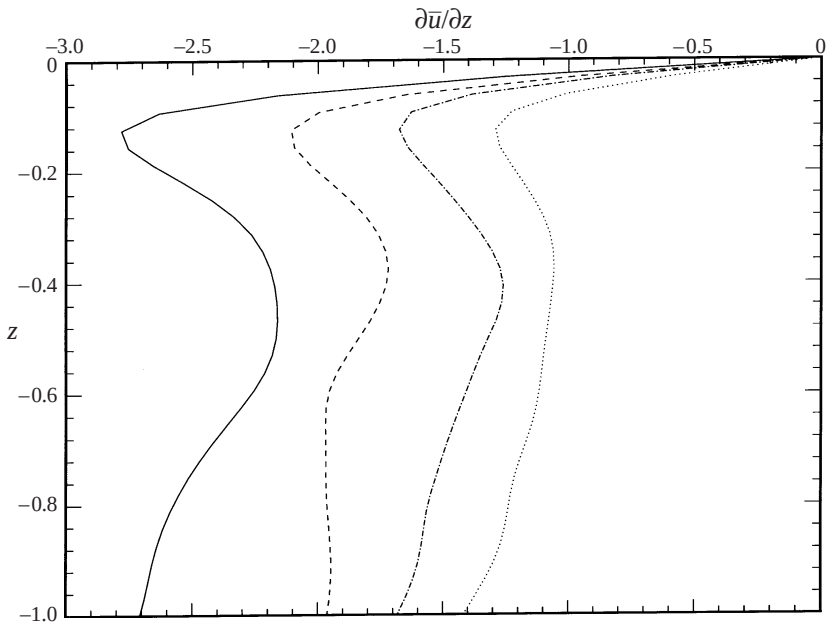

FIGURE 6. Profiles of the mean shear $\partial\overline{u}/\partial z$ at: ———, $t = 40$; – – – –, $t = 50$; – · – · –, $t = 60$; and · · · · · · ·, $t = 70$. The mean shear decreases sharply over the surface layer.

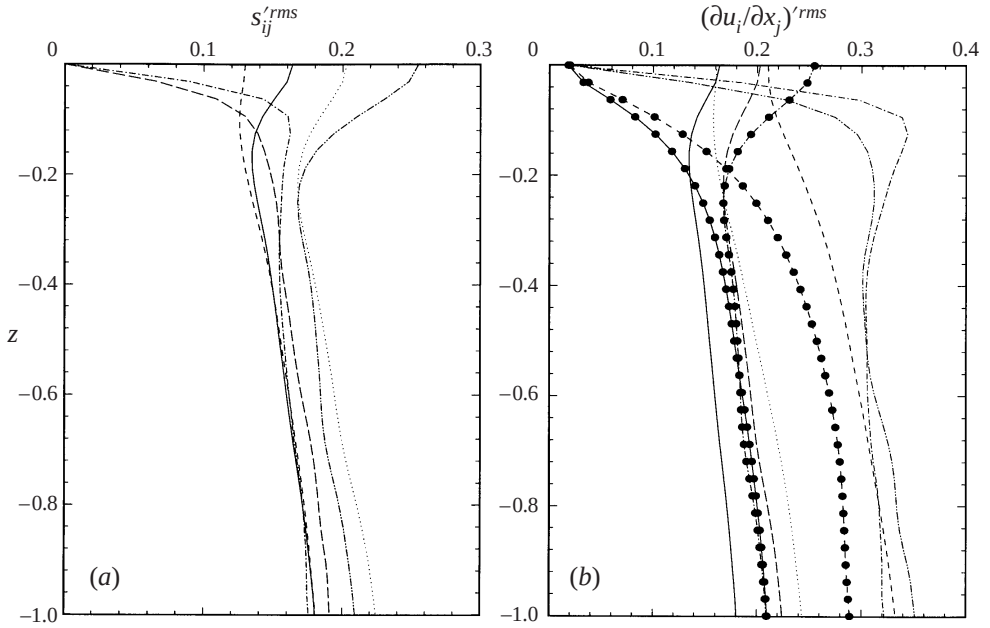

FIGURE 7. Variation of $\partial u_i/\partial x_j$ and s_{ij} over the surface layer and the blockage layer: (*a*) ———, $s_{11}^{\prime rms}$; – – – –, $s_{12}^{\prime rms}$; – · – · –, $s_{13}^{\prime rms}$; · · · · · · ·, $s_{22}^{\prime rms}$; — —, $s_{23}^{\prime rms}$; — · · — · · —, $s_{33}^{\prime rms}$. (*b*) ———, $(\partial u/\partial x)^{\prime rms}$; – – – –, $(\partial u/\partial y)^{\prime rms}$; – · – · –, $(\partial u/\partial z)^{\prime rms}$; · · · · · · ·, $(\partial v/\partial x)^{\prime rms}$; — —, $(\partial v/\partial y)^{\prime rms}$; — · · — · · —, $(\partial v/\partial z)^{\prime rms}$; —●—, $(\partial w/\partial x)^{\prime rms}$; – –●– –, $(\partial w/\partial y)^{\prime rms}$; ·●·, $(\partial w/\partial z)^{\prime rms}$. Results at $t = 60$ are plotted.

in some detail, with the focus on the surface layer since it is unique to FST. Here we demonstrate the variation of the first derivatives of velocity components $\partial u_i/\partial x_j$ and the variation of the strain components $s_{ij} \equiv (\partial u_i/\partial x_j + \partial u_j/\partial x_i)/2$ over these two layers.

The vanishing of the tangential stresses at the free surface (2.3) and (2.4) gives

$$s_{13} = s_{23} = 0 \quad \text{on} \quad z = 0, \tag{3.15}$$

and

$$\frac{\partial u}{\partial z}, \frac{\partial v}{\partial z} \ll 1 \quad \text{on} \quad z = 0. \tag{3.16}$$

Therefore, s_{13}, s_{23}, $\partial u/\partial z$, and $\partial v/\partial z$ decrease abruptly over the surface layer. This is shown in figure 7.

The term $s_{33} = \partial w/\partial z$, on the other hand, reflects the blockage effects of the surface and varies over the blockage layer. It follows from continuity that $s_{11} = \partial u/\partial x$ and $s_{22} = \partial v/\partial y$ also change over the blockage layer. In figure 7, the blockage layer depth indicated by the above variables appears to be smaller than that in figure 5(*b*) and that indicated by $\partial w/\partial x$ and $\partial w/\partial y$ in figure 7(*b*). The reason is that the flow field is inhomogeneous in the vertical direction.

The presence of the surface layer and the blockage layer can be seen in the results of previous studies. For example, Leighton *et al.* (1991), Borue *et al.* (1995), Pan & Banerjee (1995), and Walker *et al.* (1996) plot the profile of vorticity components, from which the surface layer can be observed; Handler *et al.* (1993), Borue *et al.*

(1995), Perot & Moin (1995), and Walker *et al.* (1996) plot the velocity component profiles, from which the blockage layer can be identified.

4. Vorticity dynamics in the surface layer

In this section we discuss the vorticity dynamics near the free surface, with emphasis on the role of the surface layer in the reattachment of the vorticity to the free surface.

4.1. *Free-surface observables and the underlying vortex structures*

It is known that the most prominent surface signature of FST is that due to connected normal vorticity (see e.g. Sarpkaya 1996). Figure 8 shows the contours of ω_z at the free surface at six successive time instants $t = 58$, 61, 64, 67, 70 and 73 from a specific DNS realization. Note that the (periodic) domains plotted in figure 8 are translated with the mean longitudinal velocity (cf. figure 3*a*). Coherent vortex structures are found scattered on the free surface. If we look at those vortices continuously at smaller times intervals, we can observe that a positive vortex ($\omega_z > 0$) always appears together with a negative vortex ($\omega_z < 0$) and vice versa. Figure 8 also shows that the normal vortices at the free surface are persistent with slow overall decay rates.

The presence of the aforementioned vortex structures is due to connection of vortex structures at the free surface. Using the vortex at $(-1.4, 0)$ in figure 8(f) as an example, we show how surface-connected vortices are generated. Figure 9 shows the near-surface vortex structures in a small domain of size $2 \times 2 \times 0.75$ at the four earlier time instants $t = 58$, 61, 64, and 67. The positions of these sub-domains are indicated in figures 8(a)–8(d). The vortex structures are represented by tracing a bundle of vortex lines defined as

$$\frac{\mathrm{d}\boldsymbol{x}}{\mathrm{d}\ell} = \frac{\boldsymbol{\omega}}{|\boldsymbol{\omega}|}, \tag{4.1}$$

where ℓ is the arc length of the vortex line. A fourth-order Runge–Kutta integration scheme is used to integrate (4.1).

Figure 9 also plots the contours of ω_z at the free surface above the underlying vortex structures to show their correlations.

Figure 9(a) ($t = 58$) shows the presence of a large underlying hairpin-shaped vortex structure (marked C in the figure), which is found to be prevalent in shear-flow FST. The hairpin has the 'head' near the free surface consisting mainly of near-surface horizontal vorticity and the two 'legs' in the bulk flow below. This is opposite to that in rigid-wall-turbulence case, where the legs of the hairpin are close to the boundary and the head is in the bulk flow (e.g. Moin & Kim 1985). Near the hairpin structure, in this case, there are two other vortices (marked A and B in the figure) which are already connected to the free surface.

As the hairpin vortex structure is swept towards the free surface by the uprising fluid ('splat' event), the head is dissipated quickly in the surface layer where the dissipation rate for horizontal vorticities is significantly higher. (The effects of the surface layer on vorticity dissipation are discussed in detail in § 5.3.) The hairpin vortex begins to break and the two legs connect to the free surface at the 'shoulder'. The mechanism for the connection of a hairpin vortex structure to the free surface is very much the same as the connection of, say, a vortex ring to the surface. The detailed mechanisms have been studied extensively (see e.g. Zhang, Shen & Yue 1999) and will not be repeated here.

Figure 9(b) ($t = 61$) shows such a connection occurring: part of the hairpin vortex

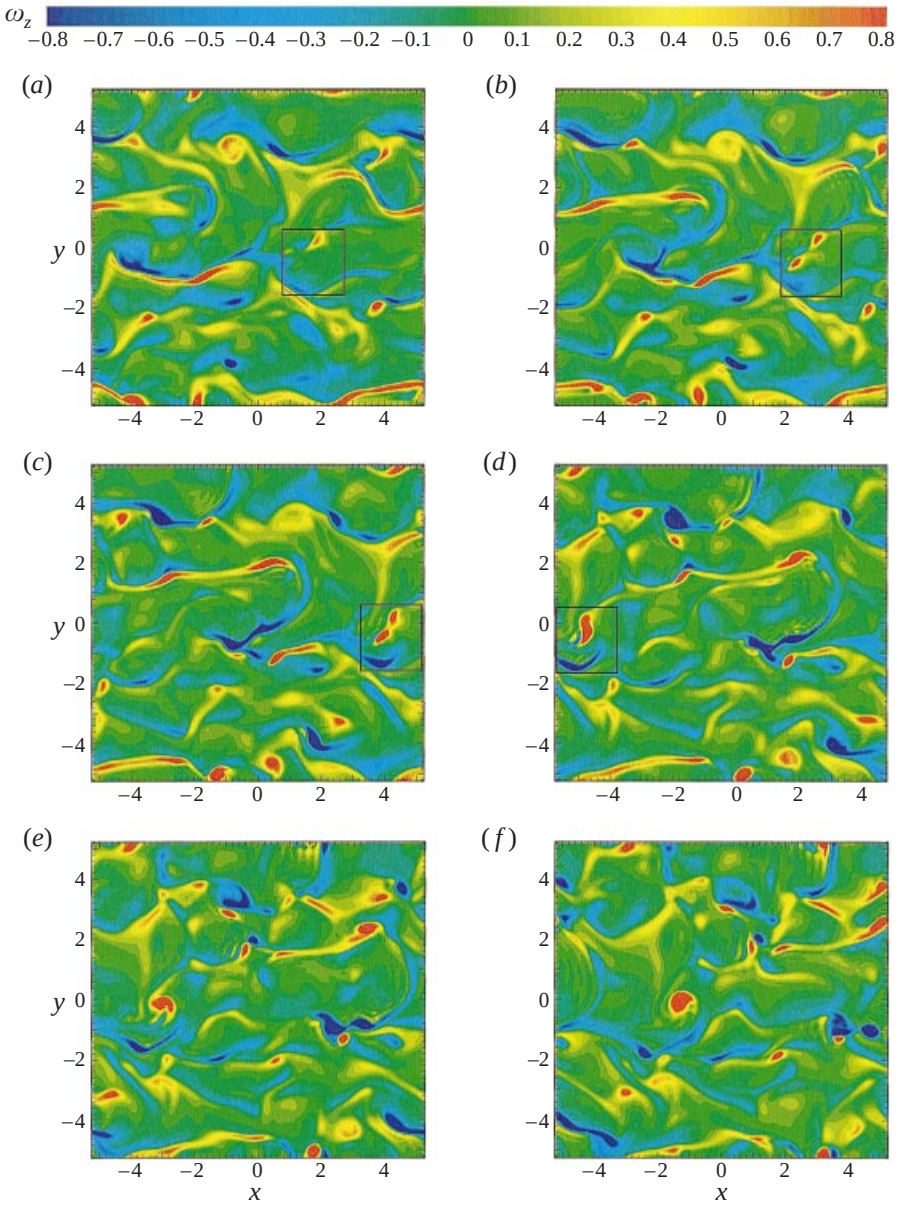

FIGURE 8. Evolution of normal vorticity at the free surface. Surface contours of ω_z are plotted at (*a*) $t = 58$; (*b*) $t = 61$; (*c*) $t = 64$; (*d*) $t = 67$; (*e*) $t = 70$; and (*f*) $t = 73$. The small boxes in (*a*) through (*d*) indicate regions where detailed vortex structures underneath are plotted in figure 9.

structure has broken and the two legs (marked C1 and C2) connect to the free surface. The remaining vortex lines of the hairpin soon also break and connect to the free surface.

The connection is complete at $t = 64$ (figure 9*c*). The two legs are completely attached to the free surface forming a pair of counter-rotating vortices with opposite signs for the ω_z component. Figure 9*c* also shows the merging of connected vortices (in this case C1 with a same-signed vortex A which had previously been connected to

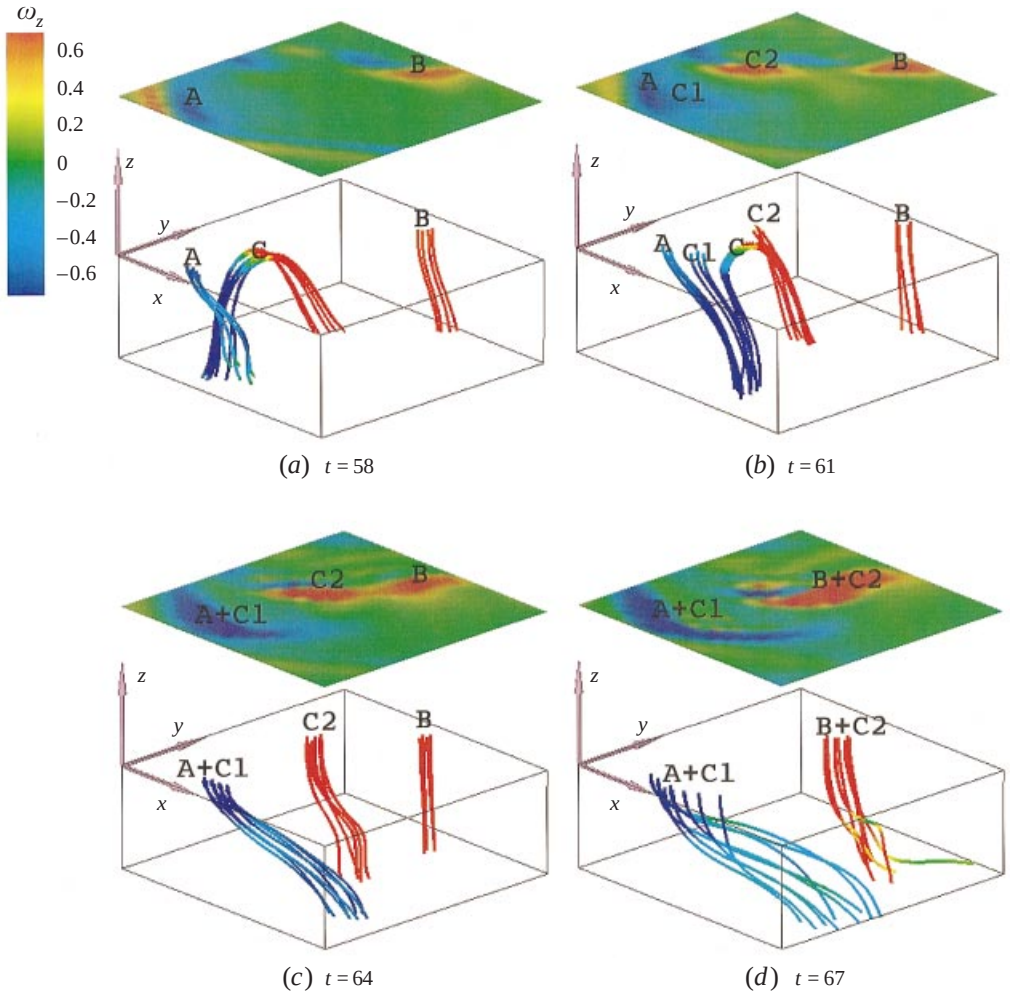

FIGURE 9. Vortex structures in shear-flow FST. Vortex lines and free surface contours of ω_z are plotted. The colours on the vortex lines represent the magnitude of ω_z. The surface contours are plotted above, which correlate with the vortex structures underneath. The domain size is $2 \times 2 \times 0.75$. The position of each domain is shown in figure 8.

the surface). At later time, $t = 67$ in figure 9(*d*), the opposite-signed leg C2 also merges with another surface-connected vortex B of that sign. This coherent vortex (B+C2) is what we see at (−1.4, 0) later at $t = 73$ (figure 8*e*). The merging of surface-connected vortices is also frequently observed in FST (e.g. Gharib, Dabiri & Zhang 1994 for grid FST; Pan & Banerjee 1995 for open-channel FST).

After the connection, vortices remain attached to the free surface and decay slowly, as shown in figure 8. In low Froude number cases, the magnitude of the horizontal vorticity components is much smaller than that of the vertical vorticity, so that the vortices are nearly perpendicular to the free surface. In the bulk flow below, the vortices are inclined in the direction of the mean shear flow.

A statistical measure of the structures and mechanisms illustrated above can be obtained by investigating the spatial distribution of two-dimensional vortex inclination angles in a way similar to Moin & Kim (1985). If the vorticity vector is projected

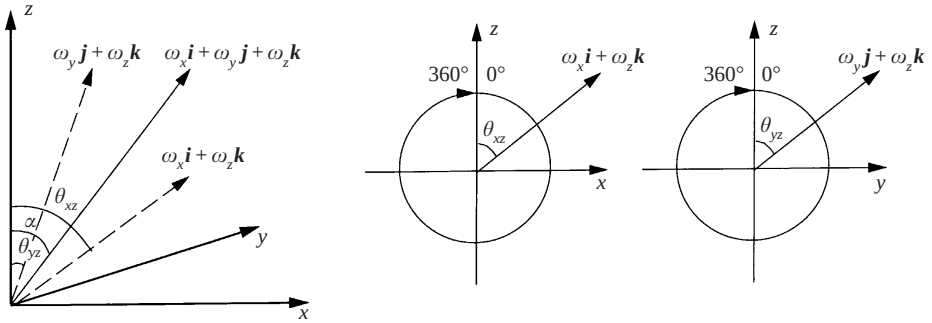

FIGURE 10. Coordinate system and sign convention for vortex inclination angles θ_{xz}, θ_{yz}, and α. θ_{xz} is the angle from the positive-z axis to $\omega_x \boldsymbol{i} + \omega_z \boldsymbol{k}$ in the (x, z)-plane; θ_{yz} is the angle from the positive-z axis to $\omega_y \boldsymbol{j} + \omega_z \boldsymbol{k}$ in the (y, z)-plane; α is the angle between the z-axis and $\omega_x \boldsymbol{i} + \omega_y \boldsymbol{j} + \omega_z \boldsymbol{k}$.

onto the (x, z)- and (y, z)-planes, the two-dimensional vortex inclination angles are defined as $\theta_{xz} = \tan^{-1}(\omega_x/\omega_z)$ and $\theta_{yz} = \tan^{-1}(\omega_y/\omega_z)$, respectively, with the sign convention for the angles and coordinate system shown in figure 10. To emphasize the stronger vortices, the inclination angles are weighted by the magnitudes of the respective projections of the vorticity vector (Moin & Kim 1985).

Figure 11(a) and 11(b) show the histograms of vortex inclination angles θ_{xz} and θ_{yz} at different depths. Near the free surface, θ_{xz} is highly concentrated around 180° and 0°/360°; while θ_{yz} is concentrated around 180°, 0°/360°, and 270°. The concentration of θ_{xz} and θ_{yz} around 180° and 0° (or 360°) indicates the dominance of vertical vorticity, which corresponds to vortices connected to the free surface, while the concentration of θ_{yz} around 270° indicates the dominance of spanwise vorticity pointing in the negative-y direction, which corresponds to the head portion of the hairpin structures. In the bulk flow ($z = -1$), the peaks of θ_{xz} shift towards 120° and 300°, which indicates that the vortices there are inclined with the mean shear flow. The concentration of θ_{yz} at 270° in the bulk reflects the spanwise vorticity of the two-dimensional mean shear flow.

Following Moin & Kim (1985), θ_{xz} and θ_{yz} in figures 11(a) and 11(b) are based on instantaneous vorticity which includes the mean vorticity of the shear flow. The two-dimensional vortex inclination angles θ'_{yz} based on instantaneous vorticity fluctuations are plotted in figure 11(c) which shows that, in the bulk flow below ($z = -1$), the concentration of θ_{yz} around 270° is absent for θ'_{yz} while near the free surface, θ_{yz} and θ'_{yz} are similar. Therefore, coherent horizontal vortex structures (head portion of coherent hairpin structures) do exist near the free surface.

We note that hairpin vortex structures and their connection to the free surface have been reported in open-channel FST (cf. Rashidi 1997), which makes the physics of shear-flow FST and open-channel FST closer to each other than to grid FST. However, the origins of the vortical events in the open-channel FST and the shear-flow FST are different. In open-channel FST, hairpin vortex structures are generated at the boundary layer at the solid bottom and are swept to the surface after ejection from the bottom. In the present flow, vorticity is generated entirely by the shear flow dynamics.

4.2. *Spatial and temporal development of the surface layer*

As we show in § 2, the surface layer is a region of rapid variations for the horizontal vorticity components and the vertical derivative of the vertical vorticity component.

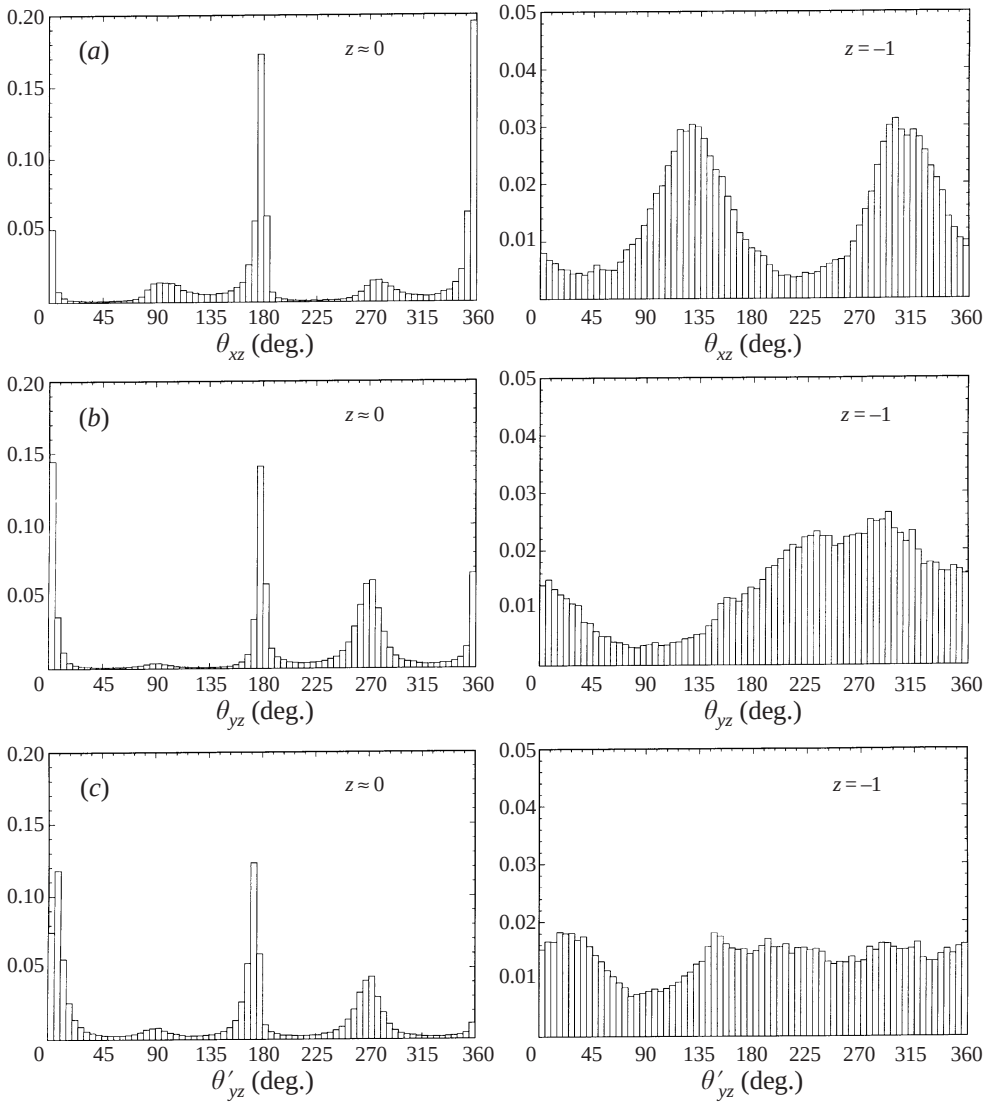

FIGURE 11. Histograms of two-dimensional vortex inclination angles near the surface and in the bulk flow below. (*a*) θ_{xz} is defined as the angle from the positive-z axis to the instantaneous vorticity $\omega_x \boldsymbol{i} + \omega_z \boldsymbol{k}$; (*b*) θ_{yz} is the angle from the positive-z axis to the instantaneous vorticity $\omega_y \boldsymbol{j} + \omega_z \boldsymbol{k}$; (*c*) θ'_{yz} is the angle from the positive-z axis to the instantaneous vorticity *fluctuation* $\omega'_y \boldsymbol{j} + \omega'_z \boldsymbol{k}$.

The surface layer is, however, not always present: for instance, a uniform flow with a free surface will have no need for a surface layer; uniform-strength vortex filaments attached perpendicularly to the free surface also satisfy the boundary conditions (2.8), (2.9), and (2.10) automatically, and the surface layer is not present. In general free-surface vortical flows, the surface layer is present whenever and wherever horizontal vortex filaments approach the free surface.

Figure 12 shows the development of the surface layer during the connection of hairpin vortex structures to the free surface. Using the hairpin vortex in § 4.1 as an example, figure 12(*a*) shows the vertical section of the hairpin structure as it approaches the free surface. The head portion of the hairpin is a region of high

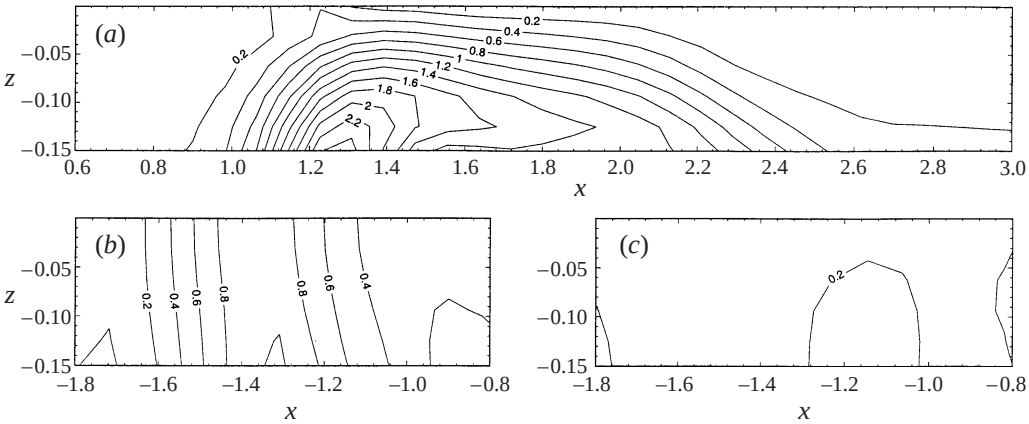

FIGURE 12. Development of the surface layer during a vortex connection process. (*a*) Contours of $(\omega_x^2 + \omega_y^2)^{1/2}$ on the vertical x, z section at $y = -0.49$, $t = 58$, when the hairpin structure in § 4.1 approaches the surface. The surface layer is evident in this case. (*b*), (*c*) Contours of $|\omega_z|$ and $(\omega_x^2 + \omega_y^2)^{1/2}$ on the vertical x, z section at $y = -0.33$, $t = 73$, when the vortex has connected to the surface. A surface layer is not present in this case. The contour intervals are 0.2 for all three figures.

horizontal vorticity (mainly ω_y) and there exist high gradients between the hairpin head and the free surface where horizontal vorticities given by (2.8) and (2.9) are small. The presence of the surface layer at, say, $x \in \sim (1.1, 2.1)$, is quite evident. Outside such a region, the vertical gradients are not large and the surface layer is absent.

After a vortex is connected to the free surface, the vertical gradients are smoothed out and the surface layer is, strictly speaking, not present. This is shown in figure 12 where the above vortex has connected to the free surface (see figure 12*b*). Figure 12(*c*) plotting the $(\omega_x^2 + \omega_y^2)^{1/2}$ contours confirms that horizontal vorticity components are small underneath and that, in general, a surface layer is absent for a vortex after it has connected to the surface.

Figure 13 shows a global picture of the spatial distribution of the surface layer. Figure 13(*a*) plots the contours of $[(\partial\omega_x/\partial z)^2 + (\partial\omega_y/\partial z)^2]^{1/2}$ at the surface $z = 0$ while figure 13(*b*) plots the contours of $(\omega_x^2 + \omega_y^2)^{1/2}$ at $z = -0.1$. In both figures, the presence of the surface layer is indicated by dark regions where the vertical derivatives of horizontal vorticity are large. The light regions are locations where significant near-surface horizontal vorticity is absent (vorticity itself is either small or has connected to the surface there), and the surface layer is not established there.

In conclusion, a surface layer only exists when/where vortex filaments (which should contain horizontal components) approach the free surface. In the present shear-flow FST, connection of vortices to the free surface occurs frequently and the surface layer is present over a considerable portion of the free surface (see figure 13) at all times.

The occurrence of hairpin vortex structures in grid FST, on the other hand, is rarer than that in sheared FST, and the effect of the surface layer is less significant for grid FST than shear-flow FST. This is discussed in § 5.

Pan & Banerjee (1995) perform an interesting test in their DNS with two different boundary conditions at the bottom: (*a*) they first apply the usual no-slip condition at the bottom; (*b*) after the flow with no-slip bottom is fully developed, they then switch the no-slip bottom to a free-slip bottom. In case (*a*), the ejection from the

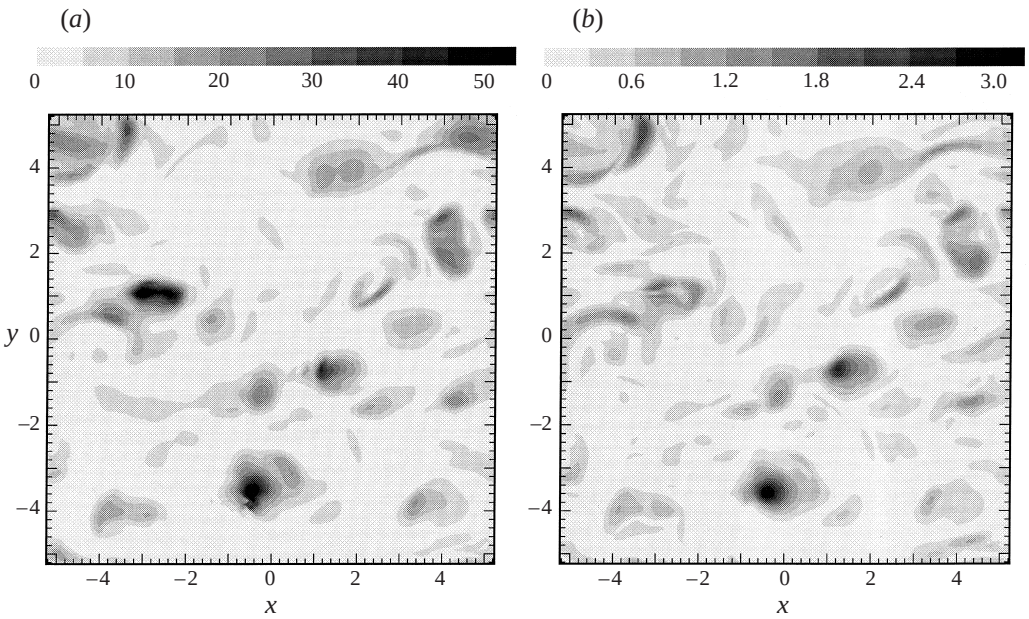

FIGURE 13. Spatial distribution of the surface layer. (*a*) Contours of $[(\partial\omega_x/\partial z)^2 + (\partial\omega_y/\partial z)^2]^{1/2}$ at $z = 0$. (*b*) Contours of $(\omega_x^2 + \omega_y^2)^{1/2}$ at $z = -0.1$. The surface layer exists at the dark regions where the vertical derivatives of horizontal vorticity are large.

wall towards the surface is found to be pronounced. In this case, we can regard the occurrence of the surface layer to be significant, since the upwelling motions sweep considerable horizontal vortex filaments (which are generated near the wall) to the surface. In case (*b*), Pan & Banerjee's (1995) results show that the mean shear flow becomes flattened out immediately and the upwellings are found to disappear. Their mean shear is much weaker than that in the present study and their flow field (*b*) is more like grid FST than the shear-flow FST here. In that case, few horizontal vortices are swept to the surface and we expect that the surface layer is less significant in case (*b*).

4.3. *Evolution of normal vorticity at the free surface*

As pointed out earlier, the surface layer has little effect on the vertical vorticity component and the surface-connected vortices are found to be extremely persistent. We analyse here the vorticity equation to reveal the underlying mechanisms for the evolution of surface-connected vortices.

The evolution equation of ω_z can be written as

$$\frac{\partial\omega_z}{\partial t} + \boldsymbol{v}\cdot\nabla\omega_z = \boldsymbol{\omega}\cdot\nabla w + \frac{1}{Re}\nabla^2\omega_z, \tag{4.2}$$

where the first term on the right represents vortex turning and stretching, and the second term vortex diffusion due to viscosity.

Defining $\nabla' \equiv (\partial/\partial x, \partial/\partial y, 0)$ and invoking continuity, we obtain

$$\frac{\partial\omega_z}{\partial t} + \nabla'\cdot(\omega_z\boldsymbol{v} - w\boldsymbol{\omega}) = \frac{1}{Re}\nabla^2\omega_z. \tag{4.3}$$

At the free surface, tangential stresses vanish as in (2.3) and (2.4):

$$\frac{\partial u}{\partial z}+\frac{\partial w}{\partial x}=\frac{\partial v}{\partial z}+\frac{\partial w}{\partial y}=0 \quad \text{on} \quad z=0. \tag{4.4}$$

It follows that

$$\nabla'\cdot(w\boldsymbol{\omega})=\frac{\partial}{\partial x}\left(\frac{\partial w^2}{\partial y}\right)-\frac{\partial}{\partial y}\left(\frac{\partial w^2}{\partial x}\right)=0 \quad \text{on} \quad z=0, \tag{4.5}$$

and (4.3) reduces to

$$\frac{\partial \omega_z}{\partial t}+\nabla'\cdot(\omega_z\boldsymbol{v})=\frac{1}{Re}\nabla^2\omega_z \quad \text{on} \quad z=0. \tag{4.6}$$

If we consider an arbitrary region $\mathscr{F}$ on the free surface, it follows from (4.6) that

$$\frac{\mathrm{d}}{\mathrm{d}t}\iint_{\mathscr{F}}\omega_z\,\mathrm{d}x\,\mathrm{d}y=\frac{1}{Re}\iint_{\mathscr{F}}\nabla^2\omega_z\,\mathrm{d}x\,\mathrm{d}y \quad \text{on} \quad z=0. \tag{4.7}$$

If $\mathscr{F}$ is taken to be the entire (periodic) domain, (4.7) becomes trivial since both integrals involving ω_z over $\mathscr{F}$ vanish.

We now consider the more general form of (4.3) under the condition (4.4). Multiplying (4.6) by $n\omega_z^{n-1}$, $n=1,2,...$, we obtain

$$\frac{\partial \omega_z^n}{\partial t}+n\omega_z^{n-1}\nabla'\cdot(\omega_z\boldsymbol{v})=\frac{n}{Re}\omega_z^{n-1}\nabla^2\omega_z \quad \text{on} \quad z=0. \tag{4.8}$$

After some manipulation we obtain

$$\frac{\partial \omega_z^n}{\partial t}+\nabla'\cdot(\omega_z^n\boldsymbol{v})=(n-1)\omega_z^n\frac{\partial w}{\partial z}+\frac{n}{Re}\omega_z^{n-1}\nabla^2\omega_z \quad \text{on} \quad z=0. \tag{4.9}$$

In the region $\mathscr{F}$ we have

$$\frac{\mathrm{d}}{\mathrm{d}t}\iint_{\mathscr{F}}\omega_z^n\,\mathrm{d}x\,\mathrm{d}y=(n-1)\iint_{\mathscr{F}}\omega_z^n\frac{\partial w}{\partial z}\mathrm{d}x\,\mathrm{d}y+\frac{n}{Re}\iint_{\mathscr{F}}\omega_z^{n-1}\nabla^2\omega_z\,\mathrm{d}x\,\mathrm{d}y \quad \text{on} \quad z=0. \tag{4.10}$$

Therefore, for $n>1$, $\iint_{\mathscr{F}}\omega_z^n\,\mathrm{d}x\,\mathrm{d}y$ over the entire free surface, is, in general, no longer conserved. Of special interest is the case $n=2$ which governs the enstrophy:

$$\begin{aligned}
&\frac{\mathrm{d}}{\mathrm{d}t}\iint_{\mathscr{F}}\omega_z^2\,\mathrm{d}x\,\mathrm{d}y\\
&\quad=\iint_{\mathscr{F}}\omega_z^2\frac{\partial w}{\partial z}\mathrm{d}x\,\mathrm{d}y+\frac{2}{Re}\iint_{\mathscr{F}}\omega_z\nabla^2\omega_z\,\mathrm{d}x\,\mathrm{d}y\\
&\quad=\underbrace{\iint_{\mathscr{F}}\omega_z^2\frac{\partial w}{\partial z}\mathrm{d}x\,\mathrm{d}y}_{\text{stretching}}\underbrace{-\iint_{\mathscr{F}}\frac{2}{Re}\nabla\omega_z\cdot\nabla\omega_z\,\mathrm{d}x\,\mathrm{d}y}_{\text{dissipation}}+\underbrace{\iint_{\mathscr{F}}\frac{1}{Re}\nabla'^2\omega_z^2\,\mathrm{d}x\,\mathrm{d}y}_{\text{horizontal diffusion}}\\
&\qquad+\underbrace{\iint_{\mathscr{F}}\frac{1}{Re}\frac{\partial^2\omega_z^2}{\partial z^2}\mathrm{d}x\,\mathrm{d}y}_{\text{vertical diffusion}}.
\end{aligned} \tag{4.11}$$

In (4.11), the first term is a vortex stretching term, which produces enstrophy. The second is a dissipation term while the third is the horizontal diffusion out of the region $\mathscr{F}$. If $\mathscr{F}$ is the entire (periodic) free surface, this horizontal diffusion is exactly zero. The fourth term is the vertical diffusion of the enstrophy. Therefore, over the

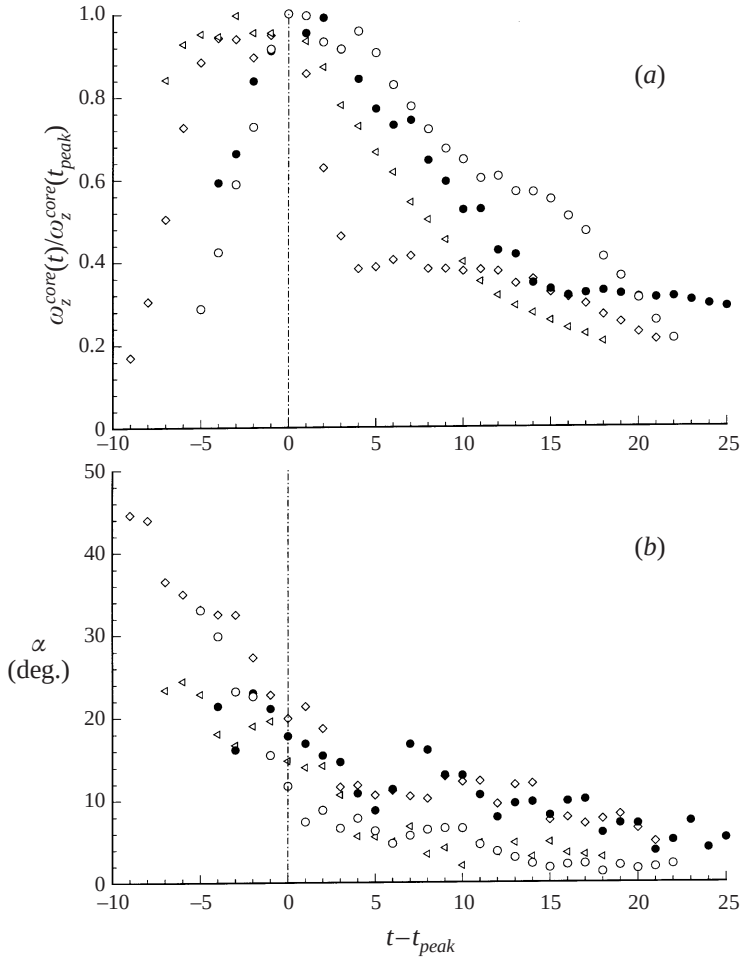

FIGURE 14. Time evolution of (*a*) core vorticity; and (*b*) surface-inclination angle α; for typical surface-connected vortices in figure 8. The vortex inclination angle for each vortex is averaged over a region defined by $\omega_z \geqslant 0.05\omega_z^{core}$, and t_{peak} is the time when ω_z^{core} reaches its maximum. Different symbols represent different connected vortices located in figure 8(*e*) (at $t = 70$) at: ◇, (−3, −0.2); ◁, (−3.8, −1.6); ○, (−1.9, 3.8); ●, (−4.6, −3.2).

entire free surface the enstrophy is in general not conserved except for a quasi-steady state in which the stretching term approximately cancels those due to dissipation and diffusion.

To investigate the evolution of surface-connected vorticity, we first examine the time evolution of the surface-inclination angle of these vortices. The three-dimensional vortex surface-inclination angle α is defined as

$$\alpha \equiv \tan^{-1}((\omega_x^2 + \omega_y^2)^{1/2}/|\omega_z|), \quad \alpha \in (0°,\ 90°), \quad z = 0, \tag{4.12}$$

i.e. α is the angle between the z-axis and the vorticity vector $\omega_x \boldsymbol{i} + \omega_y \boldsymbol{j} + \omega_z \boldsymbol{k}$, as shown in figure 10.

As expected, α is found to generally decrease as a surface-connected vortex evolves: as a vortex connects to the free surface, the horizontal components of vorticity (in the head portion of the hairpin) are not small compared to the vertical component and the inclination angle is large. After connection, the horizontal vorticity is dissipated

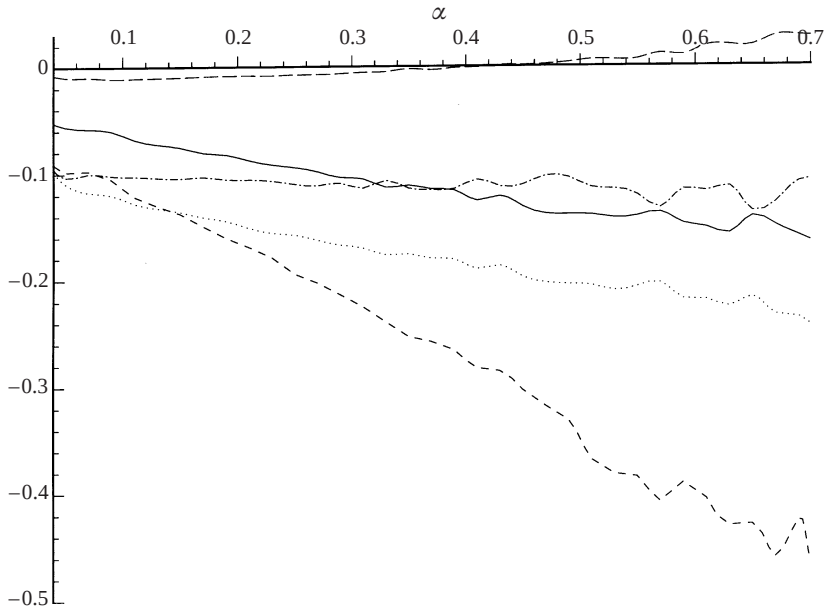

FIGURE 15. Conditional average of the evolution of surface-normal enstrophy. Terms in (4.11) normalized by ω_z^2 are plotted as function of vortex surface-inclination angle α for vortices $\omega_z \geqslant 2\omega_z^{rms}$: – – – –, (negative) stretching; ———, dissipation; – · – · –, horizontal diffusion; — —, vertical diffusion; and · · · · · · ·, dissipation for the entire free surface without the condition $\omega_z \geqslant 2\omega_z^{rms}$.

away because of the surface layer. The vertical vorticity dominates and the surface-inclination angle becomes small. This is shown in figure 14 for typical surface-connected vortices (cf. figure 8). The vortex surface-inclination angle thus provides a useful measure of the 'age' of a vortex in the connecting/connected process: large α corresponds to early stages of the evolution and small α later stages.

To examine the roles of the different terms in (4.11) in the evolution of surface-connected vortices, we perform conditional averaging over the free surface, first for $\omega_z \geqslant C\omega_z^{rms}$, where $C = 2$, say, to select the stronger surface vortices, and then for specific values of α so that the contributions at different stages of the evolution are separated: i.e. $\langle \cdot | \omega_z \geqslant 2\omega_z^{rms}; \alpha \rangle$ where $\cdot$ is a term in (4.11).

Figure 15 plots the conditional-averaged terms in (4.11) as a function of vortex surface-inclination angle α. Note that *negative* stretching, i.e. $-\int\int_{\mathscr{F}} \omega_z^2 \partial w/\partial z \, \mathrm{d}x \, \mathrm{d}y$ is plotted in figure 15. It is shown that both vortex stretching and dissipation are strongly dependent on α, and their magnitudes drop dramatically as α decreases. This is reasonable since the flow field is more three-dimensional during the early phase of connection (large α). Also at the early phase, stretching is dominant. The supplementing of enstrophy by vortex stretching exceeds the reduction due to dissipation and diffusion and therefore the enstrophy increases. At the late stage of evolution (small α), both stretching and dissipation decrease and the role of horizontal diffusion becomes more and more important. (Note that due to conditional averaging, there always exists horizontal diffusion into the area where vorticity is weaker.) The vertical diffusion is always negligible.

The disparate behaviours of vortex stretching at different stages of connection is manifested in figure 16 which plots the surface contours of ω_z, $\partial w/\partial z$, and $\omega_z^2 \partial w/\partial z$, as well as the underlying vortex lines for the vortex examined in § 4.1 at respectively $t =$

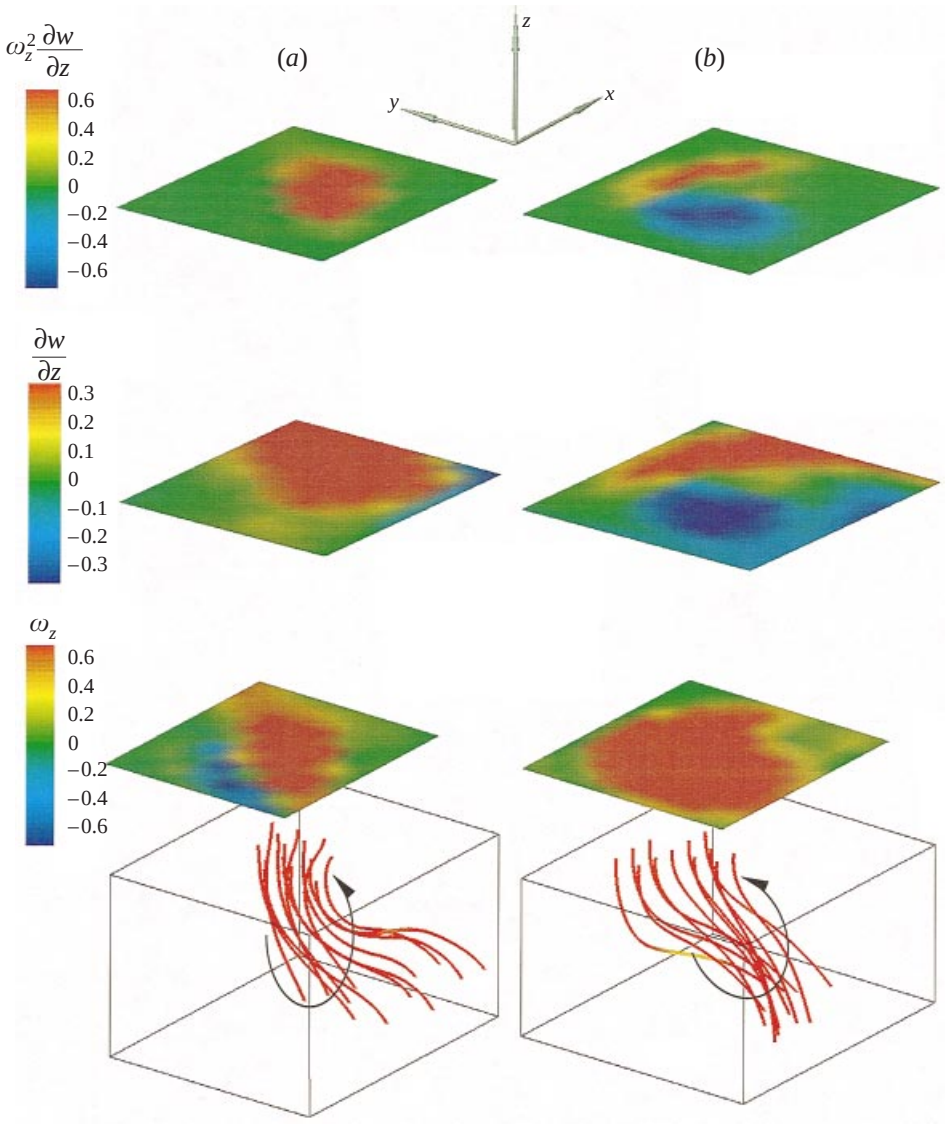

FIGURE 16. Vortex stretching for a surface-connected vortex at different stages of evolution. The vortex presented here is the one elucidated in § 4.1. Surface contours of ω_z, $\partial w/\partial z$, and $\omega_z^2 \partial w/\partial z$ and the underlying vortex lines are plotted at (*a*) $t = 64$ (early stage of evolution) and (*b*) $t = 73$ (late stage of evolution).

64 (early stage of evolution) and $t = 73$ (late stage). Note that the strain rate $\partial w/\partial z$, which governs vortex stretching, is always positive for the whole surface-connected vortex during the early stage of evolution but becomes small when integrated over the vortex at a later stage. The latter is controlled by the underlying vortex structure which generally does not remain (nearly) perpendicular to the free surface in the shear flow below. The induced strain rate over the surface connection region is thus in general approximately antisymmetric with a small net integral. This is illustrated in figure 16(*b*). The overall consequence is that vortex stretching $\int\int_{\mathscr{F}} \omega_z^2 \partial w/\partial z \, \mathrm{d}x \, \mathrm{d}y$ is strong/weak during the early/late stage of the connection. The decrease of both

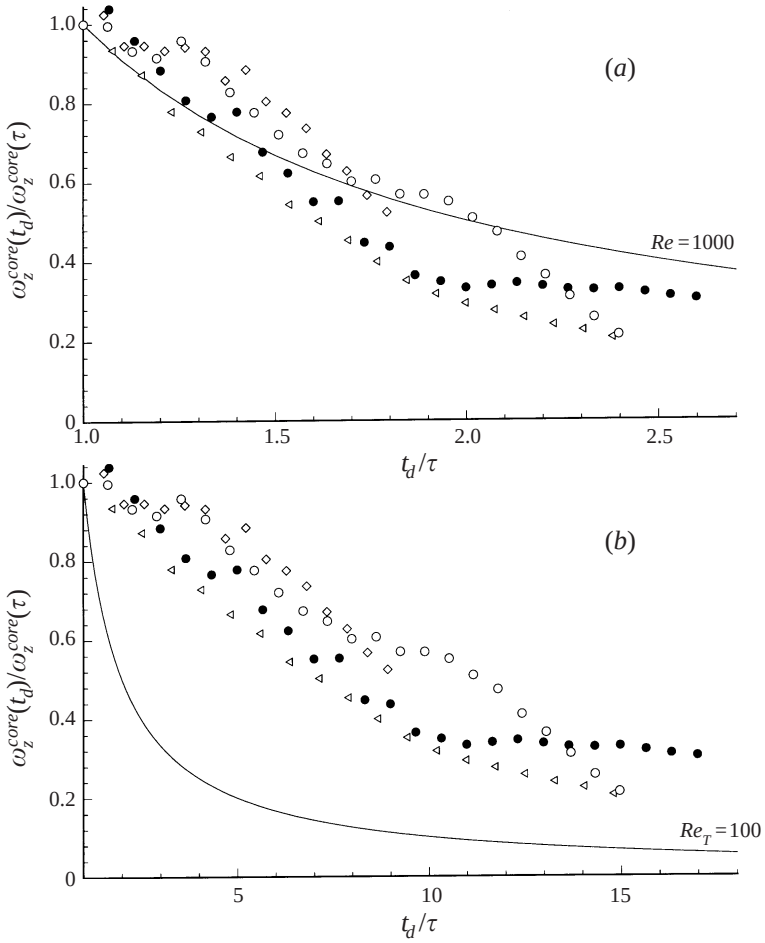

FIGURE 17. Comparison of the decay rate between surface-connected vortices and a two-dimensional Lamb laminar vortex which is at (*a*) the same Reynolds number $Re = 1000$; and (*b*) $Re_T \approx 100$ based on eddy viscosity. The symbols represent different surface-connected vortices in figure 8 whose positions are given in figure 14.

vortex stretching and viscous dissipation in the later phase makes horizontal viscous diffusion relatively important.

It is instructive to compare the evolution of a surface-connected vortex to that predicted by a two-dimensional Lamb laminar vortex which has an analytical solution for the vorticity given by

$$\omega(r, t_d) = \frac{\Gamma Re}{4\pi t_d} e^{-r^2 Re/4t_d}, \tag{4.13}$$

where r is the distance from the vortex centre, Γ the total circulation, and t_d the decay time. The vorticity at the centre ω^{core} is given by

$$\omega^{core}(t_d) = \frac{\Gamma Re}{4\pi t_d}. \tag{4.14}$$

To effect comparison, we define an initial time t' for the connected vortex using the criterion $\alpha \leqslant 20°$, obtain Γ by the integration of ω_z over the region $\omega_z \geqslant 0.05\omega_z^{core}$ at

that time, and obtain the time scale $\tau = t_d$ by solving (4.14) using these values and the observed ω^{core} at this (initial) time. The diffusion time is then given by $t_d = t - t' + \tau$.

Figure 17 compares the decay rates of surface-connected vortices to that of a Lamb vortex (solid line) assuming either the actual Reynolds number $Re = 1000$ (figure 17*a*), or one based on eddy viscosity (figure 3*a*) with Reynolds number $Re_T \approx 100$ (figure 17*b*). The figures show that the decay rate of surface-connected vortices is substantially slower than that predicted by eddy viscosity and is in fact more comparable to that due to laminar diffusion (at $Re = 1000$). This reflects the fact that for a vortex which has connected to the surface, dissipation is small as shown in figure 15 (the dissipation for strong coherent vortices, say conditioned by $\omega_z \geqslant 2\omega_z^{rms}$, is even smaller than the average value for all vortices.) The conclusion is that, relative to surface-parallel vorticity which dissipates rapidly in the surface layer, connected surface-normal vortices decay slowly and thus remain persistent on the surface. This persistence of connected vortices has been reported in experiments, see e.g. Sarpkaya (1996).

We point out that vortex stretching remains a dominant process during most of vortex connection and the net effect diminishes only as the connection is established (what net effects that remain help maintain the strength of the connected vorticity). The three-dimensional effects associated with vortex stretching are thus an important aspect of FST and quasi-two-dimensional hypotheses (e.g. Gharib *et al.* 1994; Pan & Banerjee 1995) do not in general obtain. The three-dimensionality of FST is also argued by Walker *et al.* (1996) who base their conclusion solely on turbulence statistics, which we discuss in the next section.

5. Turbulence statistics

In this section we discuss the roles of the surface layer and the blockage layer in the statistics of turbulence scales, Reynolds-stress balance, and enstrophy dynamics.

5.1. *Turbulence scales*

The velocity two-point correlation function is defined as

$$R_{lm}(r, z) = \frac{\overline{u_l(\boldsymbol{x}_p)u_l(\boldsymbol{x}_p + \boldsymbol{e}_m r)}}{\overline{u_l'^2}}, \quad l = 1, 2, 3, \quad m = 1, 2, \tag{5.1}$$

where $\boldsymbol{e}_m$ is the unit vector in the m-direction and r the distance between the two points. Summation notation is *not* implied for $l = 1, 2, 3$.

The Taylor microscale is

$$\lambda_{lm}(z) = \left[-\frac{2}{(\partial^2 R_{lm}(r, z)/\partial r^2)\,|_{r=0}}\right]^{1/2} = \left[\frac{2\overline{u_l'^2}}{\overline{(\partial u_l'/\partial x_m)^2}}\right]^{1/2}. \tag{5.2}$$

Figure 18 plots the vertical variations of Taylor microscales λ_{lm}. The streamwise scale associated with the spanwise velocity λ_{21} and the spanwise scale associated with the streamwise velocity λ_{12} increase as the free surface is approached. This phenomenon is consistent with what Handler *et al.* (1993) find (although the rate of increase in shear-flow FST here is smaller than that in open-channel FST). To explain it, Handler *et al.* (1993) propose a 'pancake' model which states that eddy

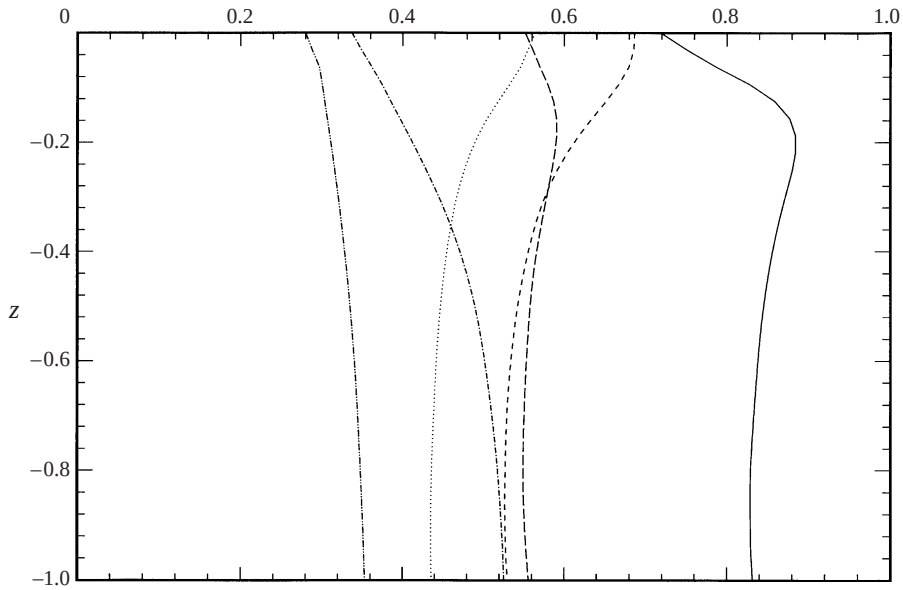

FIGURE 18. Vertical variations of Taylor microscales: ———, λ_{11}; – – – –, λ_{21}; – · – · –, λ_{13}; · · · · · · ·, λ_{12}; — —, λ_{22}; — · · — · · —, λ_{32}.

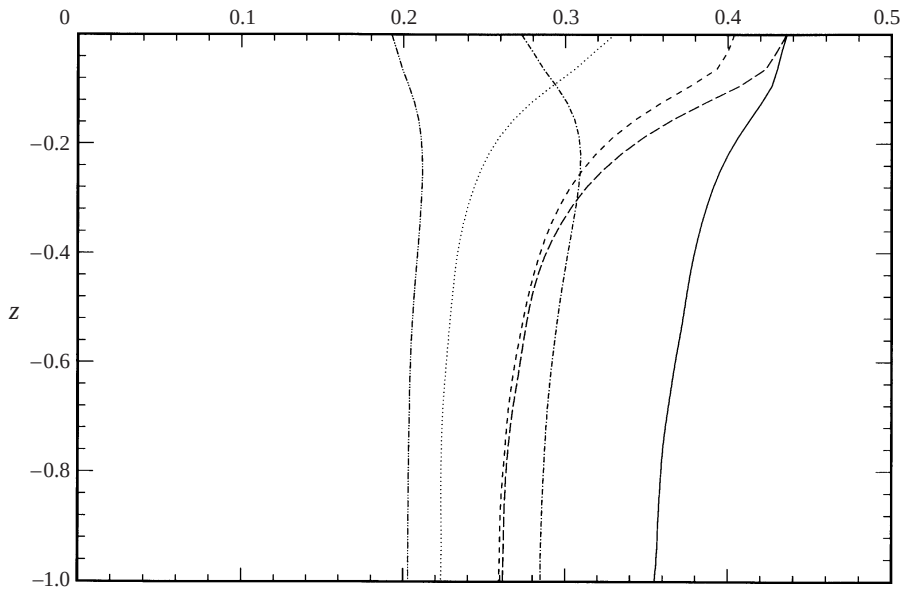

FIGURE 19. Vertical variations of Taylor microscales for vorticity: ———, λ^{ω}_{11}; – – – –, λ^{ω}_{21}; – · – · –, λ^{ω}_{13}; · · · · · · ·, λ^{ω}_{12}; — —, λ^{ω}_{22}; — · · — · · —, λ^{ω}_{32}.

structures get flattened as they impinge the free surface. To show this picture more clearly, we look at the Taylor microscale λ^{ω}_{lm} which is defined in terms of vorticity instead of velocity in (5.2). As shown in figure 19, the scales of horizontal vorticity increase within the blockage layer. The decrease of vertical vorticity scales is believed to be caused by the stretching of surface-normal vorticity.

Thus, the vertical variations of Taylor microscales (of velocity, and especially of

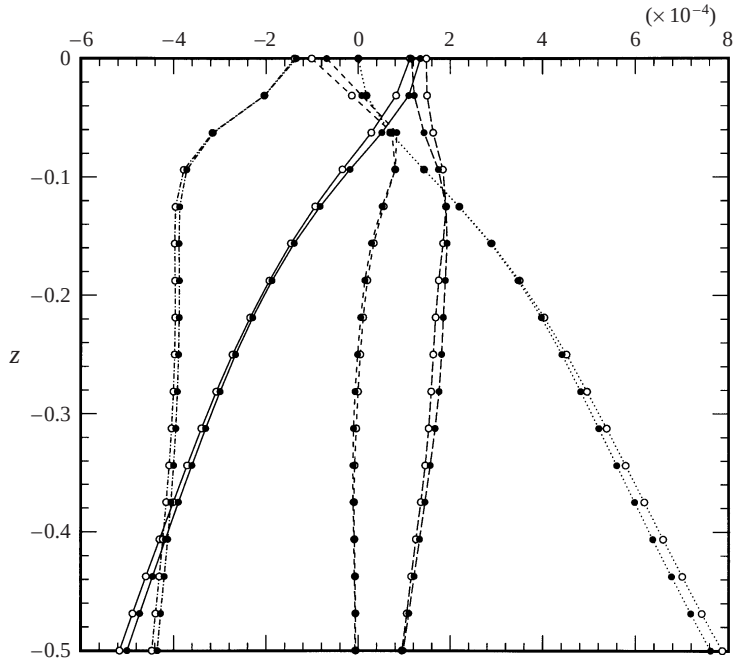

FIGURE 20. Terms in the Reynolds-stress equation for $\overline{u'^2}$: ———, pressure–strain correlation term $2\overline{p'\partial u'/\partial x}$; – – – –, viscous diffusion term $(1/Re)\partial^2\overline{u'^2}/\partial z^2$; – · – · –, dissipation term $-(2/Re)\overline{\partial u'/\partial x_k \cdot \partial u'/\partial x_k}$; — —, transport term $-\partial\overline{u'^2w'}/\partial z$; · · · · · ·, shear flow production term $-2\overline{u'w'}\partial\overline{u}/\partial z$. The symbol ○ corresponds to $Fr = 0.7$ and ● to $Fr = 0$. Froude number effects are discussed in § 6.

vorticity) support the 'pancake' model proposed by Handler *et al.* (1993). Apparently, the 'pancake' (vortex structure) gets flattened because of the blockage effect of the surface when it is swept to the surface by upwelling motions. Therefore, the 'pancake' model is a result of the blockage layer.

5.2. *Reynolds-stress balance*

For FST with a two-dimensional mean shear, the equations for the primary components of the Reynolds stresses $\overline{u'^2}$, $\overline{v'^2}$ and $\overline{w'^2}$ are (see e.g. Hinze 1975, p. 323)

$$\frac{\partial\overline{u'^2}}{\partial t} = \underbrace{2\overline{p'\frac{\partial u'}{\partial x}}}_{\text{I}} + \underbrace{\frac{1}{Re}\frac{\partial^2\overline{u'^2}}{\partial z^2}}_{\text{II}} \underbrace{-\frac{2}{Re}\overline{\frac{\partial u'}{\partial x_k}\frac{\partial u'}{\partial x_k}}}_{\text{III}} \underbrace{-\frac{\partial}{\partial z}\overline{u'^2w'}}_{\text{IV}} \underbrace{-2\overline{u'w'}\frac{\partial\overline{u}}{\partial z}}_{\text{V}}, \tag{5.3}$$

$$\frac{\partial\overline{v'^2}}{\partial t} = \underbrace{2\overline{p'\frac{\partial v'}{\partial y}}}_{\text{I}} + \underbrace{\frac{1}{Re}\frac{\partial^2\overline{v'^2}}{\partial z^2}}_{\text{II}} \underbrace{-\frac{2}{Re}\overline{\frac{\partial v'}{\partial x_k}\frac{\partial v'}{\partial x_k}}}_{\text{III}} \underbrace{-\frac{\partial}{\partial z}\overline{v'^2w'}}_{\text{IV}}, \tag{5.4}$$

$$\frac{\partial\overline{w'^2}}{\partial t} = \underbrace{2\overline{p'\frac{\partial w'}{\partial z}}}_{\text{I}} + \underbrace{\frac{1}{Re}\frac{\partial^2\overline{w'^2}}{\partial z^2}}_{\text{II}} \underbrace{-\frac{2}{Re}\overline{\frac{\partial w'}{\partial x_k}\frac{\partial w'}{\partial x_k}}}_{\text{III}} \underbrace{-\frac{\partial}{\partial z}\overline{w'^3} - 2\frac{\partial}{\partial z}\overline{p'w'}}_{\text{IV}}. \tag{5.5}$$

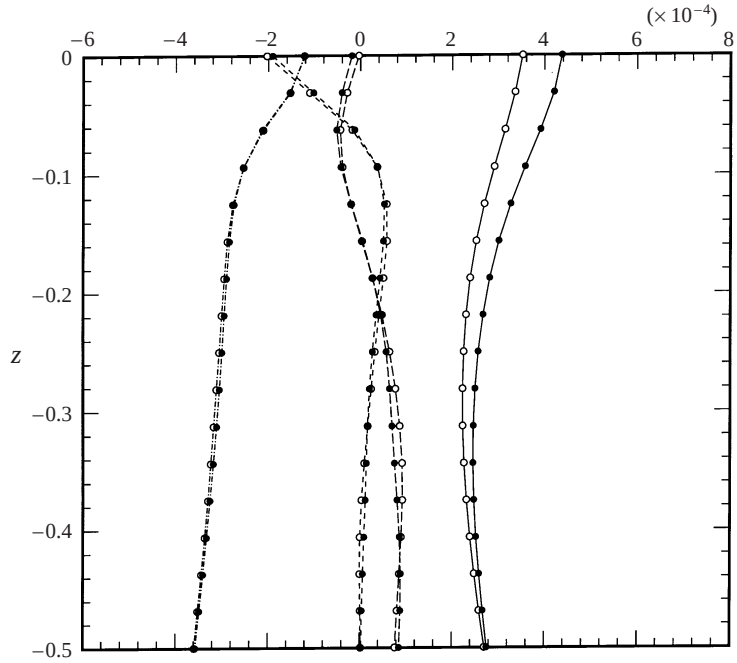

FIGURE 21. Terms in the Reynolds-stress equation for $\overline{v'^2}$: ———, pressure–strain correlation term $2\overline{p'\partial v'/\partial y}$; ----, viscous diffusion term $(1/Re)\partial^2\overline{v'^2}/\partial z^2$; – · – · –, dissipation term $-(2/Re)\overline{\partial v'/\partial x_k \cdot \partial v'/\partial x_k}$; – –, transport term $-\partial\overline{v'^2 w'}/\partial z$. The symbol ○ corresponds to $Fr = 0.7$ and ● to $Fr = 0$. Froude number effects are discussed in § 6.

Here I are the pressure–strain correlation terms, II the viscous diffusion terms, III the dissipation terms, IV the transport terms, and V the shear flow production terms.

Figures 20–22 show the vertical profiles of the above terms. Most are similar to those in open-channel FST (Handler *et al.* 1993). Compared with grid FST, however, many are qualitatively different.

Turbulence production

A fundamental difference between shear-flow FST (or open-channel FST) and grid FST is that the former has turbulence production from the mean shear while the latter purely decays. For the two-dimensional mean shear $\overline{u}(z)$ studied in this paper, (5.3)–(5.5) show that only the u' equation has the production term $-2\overline{u'w'}\partial\overline{u}/\partial z$, which means that only the streamwise velocity component obtains energy directly from the mean shear flow. Therefore, u' is larger than v' and w', which is shown in figure 5(*b*).

Figure 20 shows that turbulence production decreases as the free surface is approached. This decrease is a result of two effects: (i) the reduction of the vertical velocity w', as a result of the blockage effect, as the free surface is approached; and (ii) more importantly, the reduction of the mean velocity shear $\partial\overline{u}/\partial z$ inside the surface layer. In fact, at the free surface, the mean shear becomes zero in accordance with the zero mean stress requirement at $z = 0$.

Dissipation

For the dissipation term, there is a significant reduction within the surface layer for both the horizontal components u' and v' (figures 20 and 21). The decrease in the

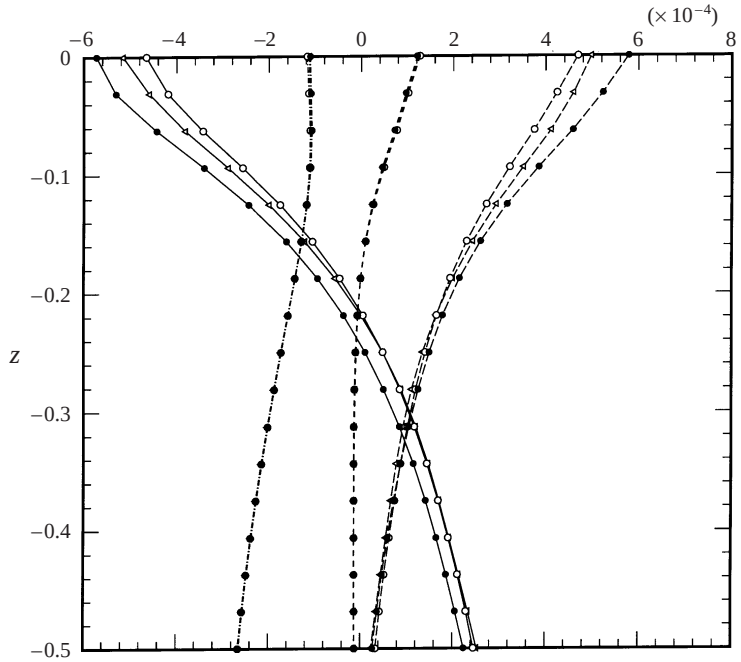

FIGURE 22. Terms in the Reynolds-stress equation for $\overline{w'^2}$: ———, pressure–strain correlation term $2\overline{p'\partial w'/\partial z}$; ----, viscous diffusion term $(1/Re)\partial^2\overline{w'^2}/\partial z^2$; – · – · –, dissipation term $-(2/Re)\overline{\partial w'/\partial x_k \cdot \partial w'/\partial x_k}$; – –, transport term $-\partial\overline{w'^3}/\partial z - 2\partial\overline{p'w'}/\partial z$. The symbol ○ corresponds to $Fr = 0.7$, ◁ to $Fr = 0.35$ and ● to $Fr = 0$. Froude number effects are discussed in § 6.

dissipation is a direct result of the zero stress condition at the free surface. More specifically, if we write explicitly the expression for the dissipation, say for the u' component,

$$-\frac{2}{Re}\overline{\frac{\partial u'}{\partial x_k}\frac{\partial u'}{\partial x_k}} = -\frac{2}{Re}\overline{\left(\frac{\partial u'}{\partial x}\right)^2} - \frac{2}{Re}\overline{\left(\frac{\partial u'}{\partial y}\right)^2} - \frac{2}{Re}\overline{\left(\frac{\partial u'}{\partial z}\right)^2}, \tag{5.6}$$

we see from § 3.5 that the value of $\partial u'/\partial x$ increases over the blockage layer and the variation of $\partial u'/\partial y$ is small. It is the last term $\partial u'/\partial z$ that must decrease abruptly inside the surface layer to reach the value dictated by the boundary condition (3.16), which is shown in figure 7(*b*). The reduction in the overall dissipation is thus due to the decrease of this term near the free surface.

Unlike in figures 20 and 21, the surface layer has no visible effect on the dissipation of w' (figure 22). The dissipation for the w' component is

$$-\frac{2}{Re}\overline{\frac{\partial w'}{\partial x_k}\frac{\partial w'}{\partial x_k}} = -\frac{2}{Re}\overline{\left(\frac{\partial w'}{\partial x}\right)^2} - \frac{2}{Re}\overline{\left(\frac{\partial w'}{\partial y}\right)^2} - \frac{2}{Re}\overline{\left(\frac{\partial w'}{\partial z}\right)^2}. \tag{5.7}$$

Figure 7(*b*) shows that over the blockage layer, $\partial w'/\partial x$ and $\partial w'/\partial y$ decrease while $\partial w'/\partial z$ increases. Thus the surface layer has little effect on the dissipation of w'.

If we now sum the dissipation of u', v', and w', we obtain the conclusion that the

total turbulent kinetic energy dissipation

$$\epsilon = \frac{1}{Re}\left(\overline{\frac{\partial u'}{\partial x_k}\frac{\partial u'}{\partial x_k} + \frac{\partial v'}{\partial x_k}\frac{\partial v'}{\partial x_k} + \frac{\partial w'}{\partial x_k}\frac{\partial w'}{\partial x_k}}\right) \tag{5.8}$$

decreases within the surface layer. Therefore most of the kinetic energy dissipation occurs outside the surface layer. This result is in contrast with the boundary layer next to a wall where the opposite is true.

The decreased dissipation at the free surface was first observed by Handler *et al.* (1993) and further discussed by Perot & Moin (1995) and Walker *et al.* (1996). Perot & Moin (1995) conjecture that the two-componentality of the turbulence near the surface and therefore the lack of the usual energy cascade leads to the reduction of dissipation. Walker *et al.* (1996) explain the reduction by the decrease of horizontal vorticity, which is in the same spirit as the present explanation (5.6) and (5.7), although their explanation is slightly more complicated. Walker *et al.* (1996) write the kinetic energy dissipation as

$$\epsilon = \frac{1}{Re}(s_{ij}s_{ji} + \tfrac{1}{2}\omega_i\omega_i), \tag{5.9}$$

and show that the decrease in dissipation results from the reduction in the enstrophy $\omega_i\omega_i$. We would like to point out that the reduction in two of the components of $s_{ij}s_{ji}$: $s_{13}s_{31}$ and $s_{23}s_{32}$, in the surface layer (figure 7*a*), also contributes to the decrease of dissipation. From our DNS data, it is found that the variation in enstrophy is responsible for about 70% of the reduction in dissipation while the variation in s_{13} and s_{23} is responsible for the remaining 30%.

Pressure–strain correlation

Since energy is extracted from the mean shear flow to u', u' is larger than v' and w'. In order to return to isotropy, energy is further transfered from u' to v' and w' through pressure–strain correlation terms. Figures 20–22 show that $2\overline{p'\partial u'/\partial x}$ is in general negative while $2\overline{p'\partial v'/\partial y}$ and $2\overline{p'\partial w'/\partial z}$ are in general positive (except near the free surface where $2\overline{p'\partial w'/\partial z}$ becomes negative). Thus u' in general loses energy to v' and w'.

Figure 22 shows that $2\overline{p'\partial w'/\partial z}$ becomes negative near the free surface, which means that w' loses energy to the two horizontal velocity components. As pointed out by Perot & Moin (1995), near the surface, the inter-component energy transfer is controlled by both splat and antisplat events: splats transfer energy from w' to u' and v' but antisplats transform the energy back immediately. It is the imbalance between the splats and antisplats that results in the inter-component energy transfer, and this imbalance is controlled by viscous processes such as dissipation and diffusion. Perot & Moin (1995) find that for grid FST, the viscous effects and therefore the inter-component energy transfer is small. The results obtained by Walker *et al.* (1996) also confirm the relatively small inter-component energy transfer in grid FST.

The situation in shear-flow FST is, however, different. If we assume that the viscous effects in sheared FST are small, as in the case of grid FST, the energy w' loses to u' and v' should be small. If we take into account the extra energy transfered from u' to v' and w' because of the mean flow production, the energy that w' loses should be even smaller (or w' may in fact gain energy). However, figure 22 shows that $2\overline{p'\partial w'/\partial z}$ is not negligible at the surface. As a matter of fact, the inter-component energy transfer is significant for sheared FST. Therefore, the imbalance between splats and antisplats near the free surface is not insignificant for shear-flow FST.

The inter-component energy transfer is also important for open-channel FST (e.g. Handler *et al.* 1993). The main difference in inter-component energy between shear-flow FST/open-channel FST and grid FST can be understood as follows: both shear-flow FST and open-channel FST are characterized by strong splat motions (which sweep horizontal vorticity filaments to the surface and make the surface layer clear) and antisplat motions, although the causes in these two types of flow are different. The former emerges from the sheared bulk flow while the latter is due to ejections from the rigid wall. Our experience in grid FST shows that splats and antisplats are quite rare compared to shear-flow FST and open-channel FST. A good example is the 'switch-bottom test' by Pan & Banerjee (1995), which we discussed in § 4.2. Therefore, the inter-component energy transfer in shear-flow FST and open-channel FST is much more important than that in grid FST.

Viscous diffusion and transport

The viscous diffusion terms in shear-flow FST are similar to those in open-channel and grid FST. Diffusion is directly related to the turbulence fluctuation profile, which is shown in figure 5(*b*). Diffusion is small in the bulk flow below and becomes comparable to other dominant terms only near the surface. For u' and v', the fluctuation increases not only because of the blockage effect of the surface, but also because of the reduction of dissipation in the surface layer. Viscous diffusion is most significant in the surface layer. Figures 20 and 21 show that diffusion transports energy from the near-surface region to the deep region for u' and v'. For w', since its profile is mainly affected by the blockage effect of the surface, diffusion is appreciable inside the blockage layer instead of the surface layer. Figure 22 shows that w' diffusion moves energy from the deep region to the surface.

The transport terms represent the vertical energy transfer due to turbulence velocity fluctuations (and pressure fluctuation in the case of w'). Since the transport terms reflect the subtle variations in the fluctuation profiles, we believe they are highly dependent on the specific problem being studied.

Finally, we remark that the summation of all the right-hand-side terms in (5.3)–(5.5), which gives the time-rate-of-change of the Reynolds stresses, is small since the near-surface region is quasi-steady. This is as expected and is in contrast with grid FST which is purely decaying.

5.3. *Enstrophy dynamics*

We have seen that the surface layer is manifest primarily in the horizontal vorticity components rather than in the vertical vorticity component. It is thus natural to expect that the surface layer will have disparate effects on the dynamics of the horizontal versus vertical enstrophy components.

The equation for the balance of the enstrophy components is given by (e.g. Tennekes & Lumley 1972 p. 87; Balint *et al.* 1988)

$$\frac{\partial\overline{\omega_x'^2}}{\partial t} = \underbrace{-\frac{\partial\overline{\omega_x'^2 w'}}{\partial z}}_{\text{II}} \underbrace{+2\overline{\left(\omega_x'^2\frac{\partial u'}{\partial x}+\omega_x'\omega_y'\frac{\partial u'}{\partial y}+\omega_x'\omega_z'\frac{\partial u'}{\partial z}\right)}}_{\text{III}} \underbrace{+2\overline{\omega_x'\omega_z'}\frac{\partial\overline{u}}{\partial z}}_{\text{IV}}$$
$$\underbrace{+2\frac{\partial\overline{u}}{\partial z}\overline{\omega_x'\frac{\partial u'}{\partial y}}}_{\text{V}} \underbrace{+\frac{1}{Re}\frac{\partial^2}{\partial z^2}\overline{\omega_x'^2}}_{\text{VI}} \underbrace{-\frac{2}{Re}\overline{\frac{\partial\omega_x'}{\partial x_k}\frac{\partial\omega_x'}{\partial x_k}}}_{\text{VII}}, \qquad (5.10)$$

$$\frac{\partial\overline{\omega_y'^2}}{\partial t} = \underbrace{-2\overline{\omega_y'w'}\frac{\partial^2\overline{u}}{\partial z^2}}_{\text{I}} \underbrace{-\frac{\partial\overline{\omega_y'^2w'}}{\partial z}}_{\text{II}} \underbrace{+2\overline{\left(\omega_x'\omega_y'\frac{\partial v'}{\partial x}+\omega_y'^2\frac{\partial v'}{\partial y}+\omega_y'\omega_z'\frac{\partial v'}{\partial z}\right)}}_{\text{III}} \underbrace{+2\frac{\partial\overline{u}}{\partial z}\overline{\omega_y'\frac{\partial v'}{\partial y}}}_{\text{V}} + \underbrace{\frac{1}{Re}\frac{\partial^2}{\partial z^2}\overline{\omega_y'^2}}_{\text{VI}} \underbrace{-\frac{2}{Re}\overline{\frac{\partial\omega_y'}{\partial x_k}\frac{\partial\omega_y'}{\partial x_k}}}_{\text{VII}}, \tag{5.11}$$

$$\frac{\partial\overline{\omega_z'^2}}{\partial t} = \underbrace{-\frac{\partial\overline{\omega_z'^2w'}}{\partial z}}_{\text{II}} \underbrace{+2\overline{\left(\omega_x'\omega_z'\frac{\partial w'}{\partial x}+\omega_y'\omega_z'\frac{\partial w'}{\partial y}+\omega_z'^2\frac{\partial w'}{\partial z}\right)}}_{\text{III}} \underbrace{+2\frac{\partial\overline{u}}{\partial z}\overline{\omega_z'\frac{\partial w'}{\partial y}}}_{\text{V}} + \underbrace{\frac{1}{Re}\frac{\partial^2}{\partial z^2}\overline{\omega_z'^2}}_{\text{VI}} \underbrace{-\frac{2}{Re}\overline{\frac{\partial\omega_z'}{\partial x_k}\frac{\partial\omega_z'}{\partial x_k}}}_{\text{VII}}. \tag{5.12}$$

Here the terms are: I, gradient production; II, transport by velocity fluctuations; III, production due to the gradients of velocity fluctuation; IV, production due to mean shear; V, mixed production; VI, viscous diffusion; and VII, dissipation.

The vertical variation of the above terms is plotted in figures 23–25. The results are largely consistent with the open-channel FST figures of Leighton *et al.* (1991). Comparing with the grid FST results (Walker *et al.* 1996), the terms related to hairpin vortex structures are different.

The most significant effects of the presence of the free surface in all these cases are the large vertical variations of the viscous diffusion term (VI) and dissipation term (VII) for the horizontal vorticity within the surface layer where vertical gradients of horizontal vorticities are high. Hence, both diffusion and dissipation increase sharply in the surface layer. In the limit of zero Froude number, it can be shown that diffusion and dissipation must be in balance at the surface (this is also true for $\overline{w'^2}$). For small Froude number, such a balance must still approximately obtain.

Unlike the horizontal enstrophy components, the viscous diffusion and dissipation terms for $\overline{\omega_z'^2}$ are not affected by the surface layer (figure 25). This is consistent with our earlier observations that the variation of ω_z is small over the surface layer since it is not ω_z but $\partial\omega_z/\partial z$ that is controlled by the surface layer.

The different behaviours of viscous diffusion/dissipation for horizontal vorticity and vertical vorticity explain the rapid vanishing of the head portion of hairpin vortices within the surface layer in contrast to the persistence of surface-connected vortices as discussed in § 4.

For the same reason, the transport term (II), which reflects the vertical variation of the intensity of vorticity fluctuation, also has disparate behaviour for horizontal and vertical vorticity components. The transport for $\overline{\omega_x'^2}$ and $\overline{\omega_y'^2}$ becomes significant in the surface layer where ω_x' and ω_y' attenuate rapidly, and ω_x' and ω_y' enstrophy is transported from below to the surface layer. The transport term for $\overline{\omega_z'^2}$, on the other hand, becomes important in the blockage layer instead of the surface layer, since the fluctuation of ω_z' varies over the blockage layer.

Both the surface layer effects and the blockage layer effects are manifest in the production due to the gradients of velocity fluctuation term (III). To show the mechanisms more clearly, figures 23(*b*), 24(*b*), and 25(*b*) plot each component of III. As shown, the production due to stretching ($2\overline{\omega_x'^2(\partial u'/\partial x)}$, $2\overline{\omega_y'^2(\partial v'/\partial y)}$, and

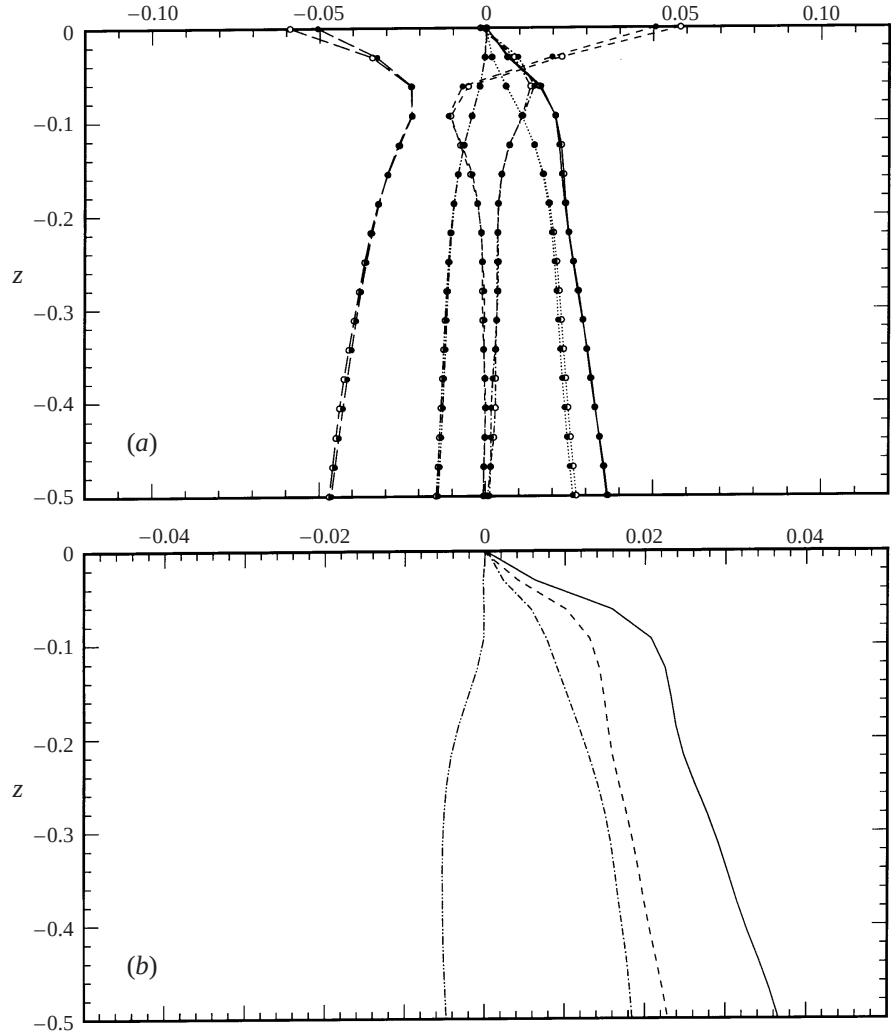

FIGURE 23. Terms in the enstrophy evolution equation for $\overline{\omega_x'^2}$: (*a*) – · – · –, transport by velocity fluctuations $-\partial\overline{\omega_x'^2 w'}/\partial z$; ———, production due to the gradients of velocity fluctuation $2\overline{(\omega_x'^2(\partial u'/\partial x) + \omega_x'\omega_y'(\partial u'/\partial y) + \omega_x'\omega_z'(\partial u'/\partial z))}$; · · · · · · ·, production due to mean shear $2\overline{\omega_x'\omega_z'}\partial\overline{u}/\partial z$; — · · — · · —, mixed production $2\overline{(\partial\overline{u}/\partial z)\omega_x'(\partial u'/\partial y)}$; – – – –, viscous diffusion $(1/Re)\partial^2\overline{\omega_x'^2}/\partial z^2$; — —, dissipation $-(2/Re)\overline{(\partial\omega_x'/\partial x_k)(\partial\omega_x'/\partial x_k)}$. (*b*) ———, The total production due to the gradients of velocity fluctuation; – – – –, $2\overline{\omega_x'^2(\partial u'/\partial x)}$; – · – · –, $2\overline{\omega_x'\omega_y'(\partial u'/\partial y)}$; — · · — · · —, $2\overline{\omega_x'\omega_z'(\partial u'/\partial z)}$. The symbol ○ corresponds to $Fr = 0.7$ and ● to $Fr = 0$. Froude number effects are discussed in § 6.

$2\overline{\omega_z'^2(\partial w'/\partial z)}$) is dominant near the surface. Their significant increase in the blockage layer is due to the increase in stretching ($\partial u'/\partial x$, $\partial v'/\partial y$, and $\partial w'/\partial z$) there. (Leighton *et al.* 1991 and Walker *et al.* 1996 explain this by using the 'splat' concept. Walker *et al.* 1996 further argue that FST is fully three-dimensional up to the surface based on the vertical stretching $\partial w'/\partial z$.)

The surface layer makes $2\overline{\omega_x'^2(\partial u'/\partial x)}$ and $2\overline{\omega_y'^2(\partial v'/\partial y)}$ different from $2\overline{\omega_z'^2(\partial w'/\partial z)}$. For horizontal components, the stretching of horizontal vorticity decreases sharply

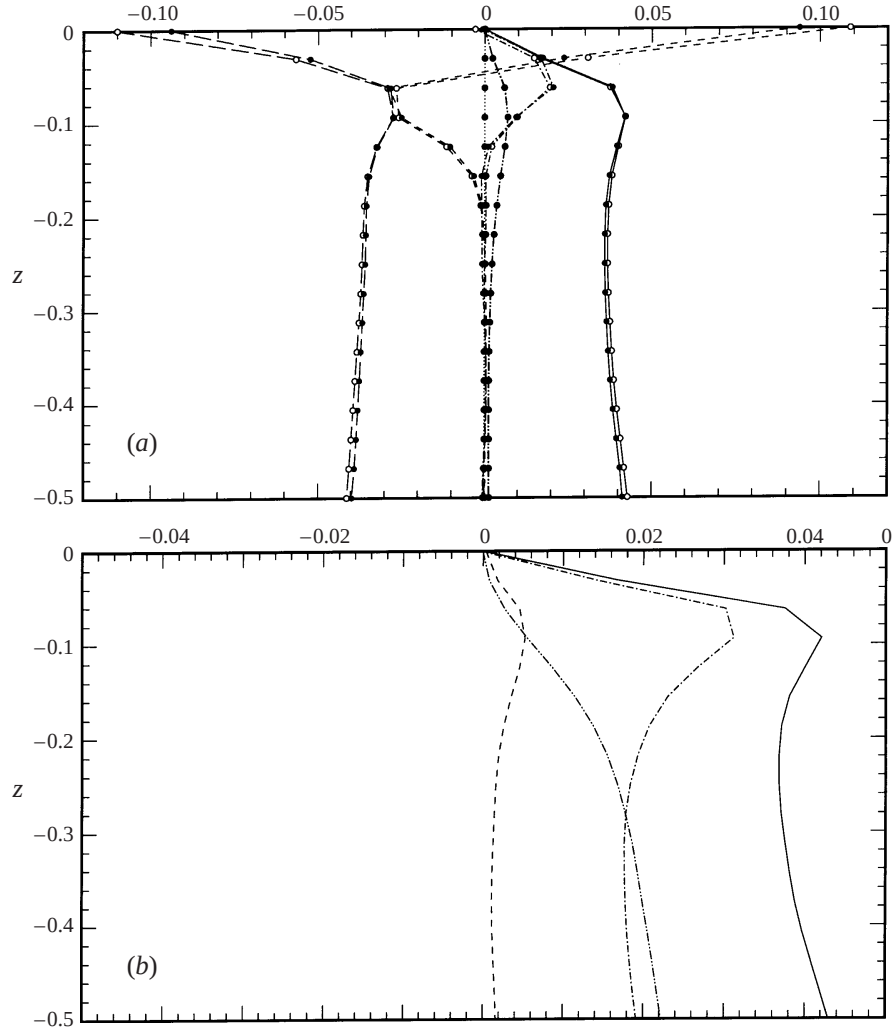

FIGURE 24. Terms in the enstrophy evolution equation for $\overline{\omega_y'^2}$: (*a*) – · – · –, transport by velocity fluctuations $-\partial\overline{\omega_y'^2 w'}/\partial z$; ———, production due to the gradients of velocity fluctuation $2\overline{(\omega_x'\omega_y'(\partial v'/\partial x) + \omega_y'^2(\partial v'/\partial y) + \omega_y'\omega_z'(\partial v'/\partial z))}$; · · · · · · ·, gradient production $-2\overline{\omega_y' w'}(\partial^2\bar{u}/\partial z^2)$; — · · — · · —, mixed production $2(\partial\bar{u}/\partial z)\overline{\omega_y'(\partial v'/\partial y)}$; – – – –, viscous diffusion $(1/Re)\partial^2\overline{\omega_y'^2}/\partial z^2$; — —, dissipation $-(2/Re)\overline{(\partial\omega_y'/\partial x_k)(\partial\omega_y'/\partial x_k)}$. (*b*) ———, The total production due to the gradients of velocity fluctuation; – – – –, $2\overline{\omega_x'\omega_y'(\partial v'/\partial x)}$; – · – · –, $2\overline{\omega_y'^2(\partial v'/\partial y)}$; — · · — · · —, $2\overline{\omega_y'\omega_z'(\partial v'/\partial z)}$. The symbol ○ corresponds to $Fr = 0.7$ and ● to $Fr = 0$. Froude number effects are discussed in § 6.

over the surface layer since ω_x and ω_y diminish at the free surface. The stretching of vertical vorticity, on the other hand, continues to increase up to the free surface, since ω_z does not need to decrease in the surface layer.

An important observation is the significance of the ω_y stretching (figure 24). It increases inside the blockage layer and reaches its peak just outside the surface layer. This peak is more prominent than that of ω_x (figure 23); it is also much larger than the horizontal stretching in grid FST (Walker *et al.* 1996). The significance of the ω_y

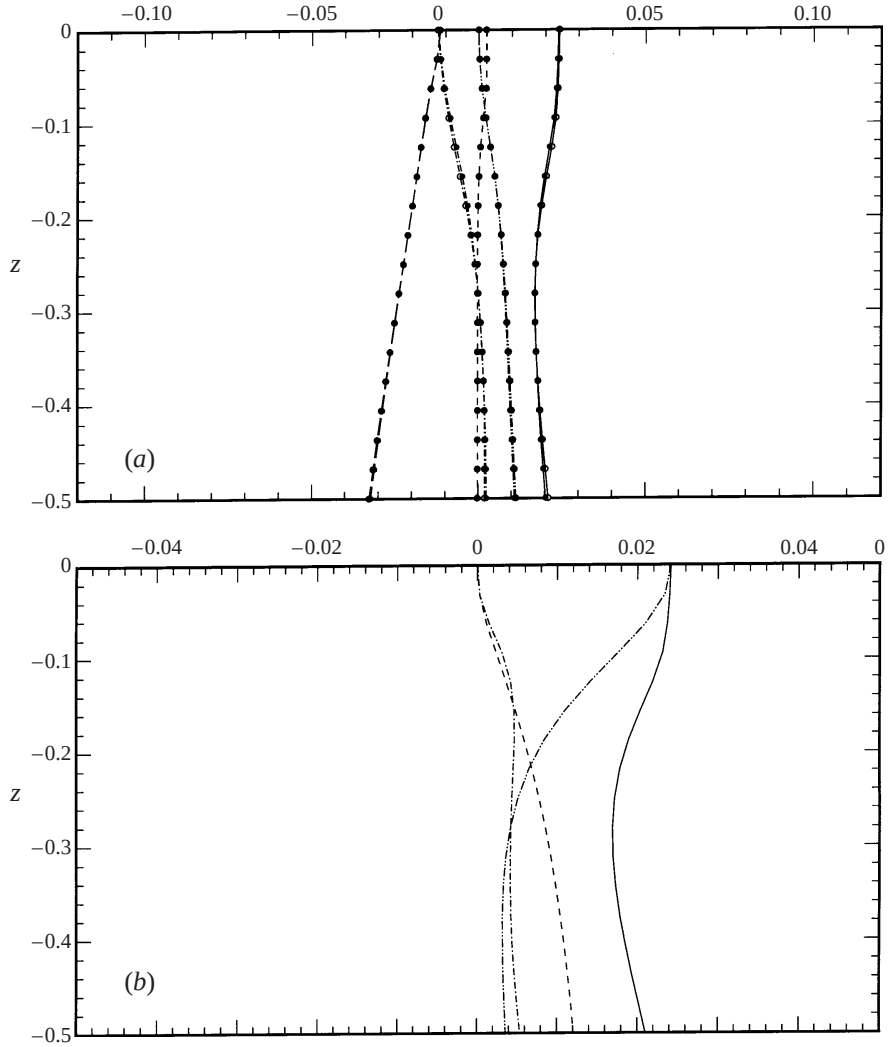

FIGURE 25. Terms in the enstrophy evolution equation for $\overline{\omega_z'^2}$: (*a*) – · – · –, transport by velocity fluctuations $-\partial\overline{\omega_z'^2 w'}/\partial z$; ———, production due to the gradients of velocity fluctuation $2\overline{(\omega_x'\omega_z'(\partial w'/\partial x) + \omega_y'\omega_z'(\partial w'/\partial y) + \omega_z'^2(\partial w'/\partial z))}$; — · · — · · —, mixed production $2(\partial\overline{u}/\partial z)\overline{\omega_z'(\partial w'/\partial y)}$; – – – –, viscous diffusion $(1/Re)\partial^2\overline{\omega_z'^2}/\partial z^2$; — —, dissipation $-(2/Re)\overline{(\partial\omega_z'/\partial x_k)(\partial\omega_z'/\partial x_k)}$. (*b*) ———, The total production due to the gradients of velocity fluctuation; – – – –, $2\overline{\omega_x'\omega_z'(\partial w'/\partial x)}$; – · – · –, $2\overline{\omega_y'\omega_z'(\partial w'/\partial y)}$; — · · — · · —, $2\overline{\omega_z'^2(\partial w'/\partial z)}$. The symbol ○ corresponds to $Fr = 0.7$ and ● to $Fr = 0$. Froude number effects are discussed in § 6.

stretching in shear-flow FST is due to the hairpin vortex structures investigated in § 4. The head portion of hairpin vortices corresponds to the enhanced spanwise vorticity ω_y, which is shown in figure 5(*b*). As the hairpin head enters the blockage layer, it is stretched by the diverging flow due to blockage effect of the surface ('pancake' model or 'splat' model). Therefore, the above difference in ω_x and ω_y stretching is consistent with the hairpin vortex structures discussed in § 4.

The remaining terms are characteristic of sheared FST and not present in grid FST. The gradient production term (I) exchanges enstrophy between the mean vorticity

and the vorticity fluctuation and only the ω_y equation has this term. The production due to mean shear (IV) is similar to the production term in the Reynolds-stress equation and only ω_x has this term. The mixed production (V) is present for all the three components of vorticity. An interesting observation from figures 23–25 is that the summation of all the mixed production for each vorticity component is close to zero, which means that the mixed production somehow redistributes the enstrophy among the vorticity components.

6. The effect of the Froude number

6.1. *Overview*

In the study of FST of small Froude numbers, it is often suggested that the free surface can be approximated as a flat free-slip plate, in which case free-slip boundary conditions apply at $z = 0$:

$$\frac{\partial u}{\partial z} = \frac{\partial v}{\partial z} = 0\,, \tag{6.1}$$

$$w = 0\,, \tag{6.2}$$

$$\frac{\partial p}{\partial z} = 0\,. \tag{6.3}$$

These obtain also from (2.3), (2.4), (2.5), and (2.7) (and (2.1)) in the limit $Fr \to 0$.

Since the free-slip-plate approximation does not involve motions of the free surface, the question remains whether free-surface effects on the turbulent flow are indeed negligible for relatively small Froude numbers. To study this, we compare our DNS results for the free-surface case ($Fr = 0.7$) with another set of (twenty) simulations under identical conditions but using free-slip-plate ($Fr = 0$) boundary conditions (6.1)–(6.3).

Table 1 shows the comparison of relevant turbulence statistics between the two cases. In table 1, $\omega_q \equiv ((\omega_x'^{rms})^2 + (\omega_y'^{rms})^2 + (\omega_z'^{rms})^2)^{1/2}$ is the fluctuation intensity of enstrophy; and $\overline{p}$ is the horizontal average of pressure which satisfies

$$\overline{p} - \overline{p}_{bottom} = -\overline{w^2} + \overline{w^2_{bottom}} = -\overline{w^2}\,. \tag{6.4}$$

Equation (6.4) is obtained by averaging the z-component of the Navier–Stokes equations (2.1) over the (x, y)-plane and integrating with respect to z.

We remark that $Fr = 0.7$ is based on the initial mean velocity deficit U. A more appropriate scale here is the turbulence velocity fluctuation at the surface $q_0 \simeq 0.1U$, which yields the Froude number $Fr_q \simeq 0.07$. Thus, the difference between the free-slip-plate turbulence and the free-surface turbulence is expected to be quite small, in particular for all the quantities considered in table 1.

The exception to the above observation turns out to be quite subtle. Figures 23 and 24 show that inside the surface layer, the variations of dissipation and diffusion for horizontal vorticity in the $Fr = 0.7$ case is slightly larger than those in the $Fr = 0$ case. This implies that the vertical gradients of horizontal vorticities increase for the $Fr = 0.7$ case. The blockage layer effects, on the other hand, are weakened by the free surface. This can be seen most clearly in figure 22: the pressure–strain correlation term and the transport term in the free-surface case are considerably smaller than those in the $Fr = 0$ case, even for such small Froude numbers.

In the following subsections, we discuss the effects of (small) Froude numbers on the surface layer and the blockage layer, respectively.

	$z = 0$		$z = -0.125$		$z = -1$	
	$Fr = 0.7$	$Fr = 0$	$Fr = 0.7$	$Fr = 0$	$Fr = 0.7$	$Fr = 0$
$\overline{u}$	0.3771	0.3763	0.3924	0.3921	0.5206	0.5221
u'^{rms}	0.8171×10^{-1}	0.8196×10^{-1}	0.8154×10^{-1}	0.8170×10^{-1}	0.1031	0.1041
v'^{rms}	0.7825×10^{-1}	0.7946×10^{-1}	0.7301×10^{-1}	0.7397×10^{-1}	0.8793×10^{-1}	0.8811×10^{-1}
w'^{rms}	0.3003×10^{-2}	0	0.2732×10^{-1}	0.2666×10^{-1}	0.7396×10^{-1}	0.7359×10^{-1}
q	0.1132	0.1139	0.1132	0.1135	0.1546	0.1549
$\omega_x'^{rms}$	0.3961×10^{-1}	0	0.3624	0.3510	0.5180	0.5073
$\omega_y'^{rms}$	0.3664×10^{-1}	0	0.3903	0.3913	0.4147	0.4382
$\omega_z'^{rms}$	0.2710	0.2656	0.2972	0.2929	0.4572	0.4527
ω_q	0.2789	0.2663	0.6122	0.6039	0.8065	0.8102
$\overline{p} - \overline{p}_{bottom}$	-0.9018×10^{-5}	0	-0.7464×10^{-3}	-0.7108×10^{-3}	-0.5470×10^{-2}	-0.5415×10^{-2}
p'^{rms}	0.8434×10^{-2}	0.8448×10^{-2}	0.8519×10^{-2}	0.8526×10^{-2}	0.1143×10^{-1}	0.1145×10^{-1}
h'^{rms}	0.4251×10^{-2}	0	—	—	—	—

TABLE 1. Comparison between free-surface turbulence ($Fr = 0.7$) and free-slip-plate turbulence ($Fr = 0$) at $t = 60$.

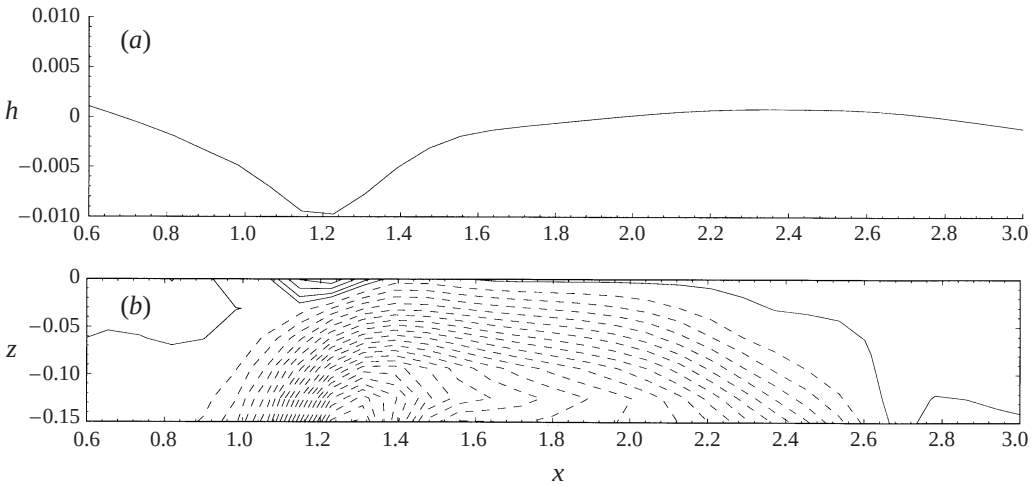

FIGURE 26. (*a*) Free-surface elevation h and (*b*) surface vorticity ω_y, induced by an underlying vortex approaching the free surface. The position and time is the same as in figure 12(*a*). In (*b*), solid lines represent positive contour values while dashed lines represent negative values. The contour increment is 0.1.

6.2. *Effects of Froude number on the surface layer*

The horizontal vorticity ω_x and ω_y at the surface is given by (2.8) and (2.9). At a free-slip plate, ω_x and ω_y are both zero. At a free surface, however, the surface vorticity components ω_x and ω_y are non-zero, although the magnitude is small for low Froude numbers.

Figure 26 shows the free-surface elevation and surface vorticity induced by an underlying vortical structure (we use, as an example, the vortex structure in figure 12*a*). The coherent vortex structure in the figure (dashed lines) is the cross-section of a hairpin head, whose ω_y component is negative. As the hairpin approaches the free surface, secondary surface vorticity is induced. This can be seen most clearly at the position ($x = 1.2,\ z = 0$). The free surface is depressed and the induced surface vorticity has a positive ω_y component, which is opposite in sign to the main vortex underneath. These observations are consistent with those for laminar vortex connection at a free surface (see e.g. Zhang *et al.* 1999).

The opposite signs of the surface vorticity and the vortex underneath which generates it is confirmed by statistics. The correlation between the vorticity at the surface and that underneath is defined as

$$Cor\langle\omega_i(0),\omega_i(z)\rangle \equiv \frac{\overline{\omega_i(0)\omega_i(z)}}{\omega_i^{rms}(0)\omega_i^{rms}(z)},\quad i=1,2,3\,, \tag{6.5}$$

where no summation notation is implied, and $\omega_i(0) \equiv \omega_i|_{z=0}$ and $\omega_i(z) \equiv \omega_i|_{z=z}$ etc.

Figure 27 plots the correlation function (6.5) for ω_x, ω_y, and ω_z. $Cor\langle\omega_z(0),\omega_z(z)\rangle$ decreases slowly over the blockage layer, which means that the surface-normal vorticity is well correlated with the vortex structures underneath. The correlation functions for ω_x and ω_y, on the other hand, decrease sharply over the surface layer which shows that the structure of horizontal vorticity changes dramatically near the free surface. This result is of fundamental importance when information from surface sensing (such as the imaging of a ship wake) is used to deduce structures of the underlying flow.

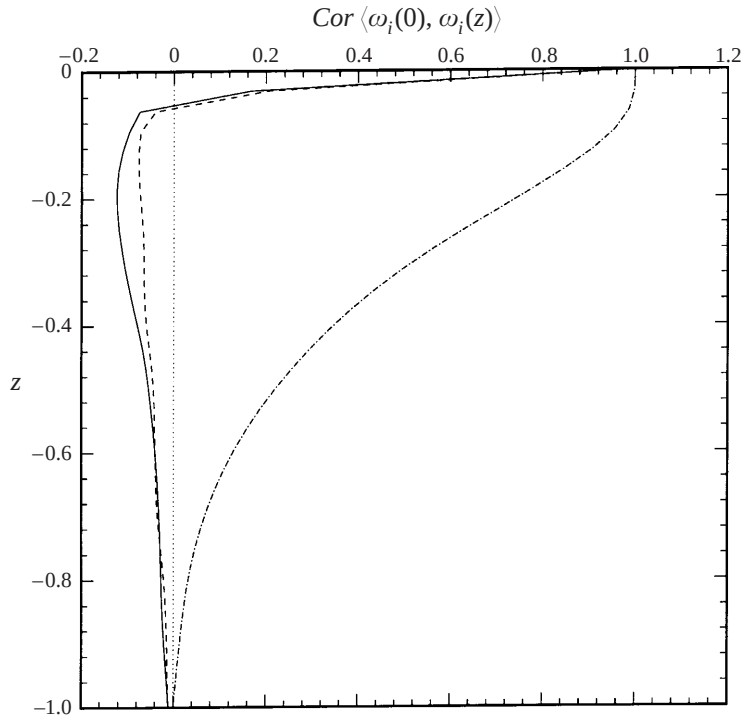

FIGURE 27. Correlation between the vorticity at the surface and vorticity underneath. ———, $Cor\langle\omega_x(0),\omega_x(z)\rangle$; – – – –, $Cor\langle\omega_y(0),\omega_y(z)\rangle$; – · – · –, $Cor\langle\omega_z(0),\omega_z(z)\rangle$.

Figure 27 shows that the correlation functions for ω_x and ω_y are negative for small z. The surface layer is the region where horizontal vorticity changes from 'outer' values to the small values at the surface layer. Comparing with the $Fr = 0$ case where surface vorticity is zero, the free surface produces surface vorticity which signs opposite to those underneath. Therefore, the vertical gradients in the free-surface case are larger than those in the free-slip-plate case. This explains why the surface layer effects are slightly larger for FST in figures 23(*a*) and 24(*a*).

It should be pointed out that surface vorticity at low Froude numbers is small compared to the vorticity of underlying vortex structures. Therefore, the effects of small Froude numbers on the surface layer is not pronounced. The Froude number effects on the blockage layer is, however, much more prominent, which we investigate next.

6.3. *Effects of Froude number on the blockage layer*

As we pointed out, quantities associated with the pressure distribution have considerable difference between the free-slip-plate turbulence and free-surface turbulence, even for small Froude numbers.

Figure 22 of § 5.2 plots the vertical variation of the terms in the Reynolds-stress equation for $\overline{w'^2}$, for both the free-surface ($Fr = 0.7$) case and the free-slip plate ($Fr = 0$) case. To provide a further check, we plot here also the results for $Fr = 0.35$. As shown in figure 22, the effects of Froude numbers on dissipation and diffusion are negligible. However, the differences in the pressure–strain correlation term and transport term are significant.

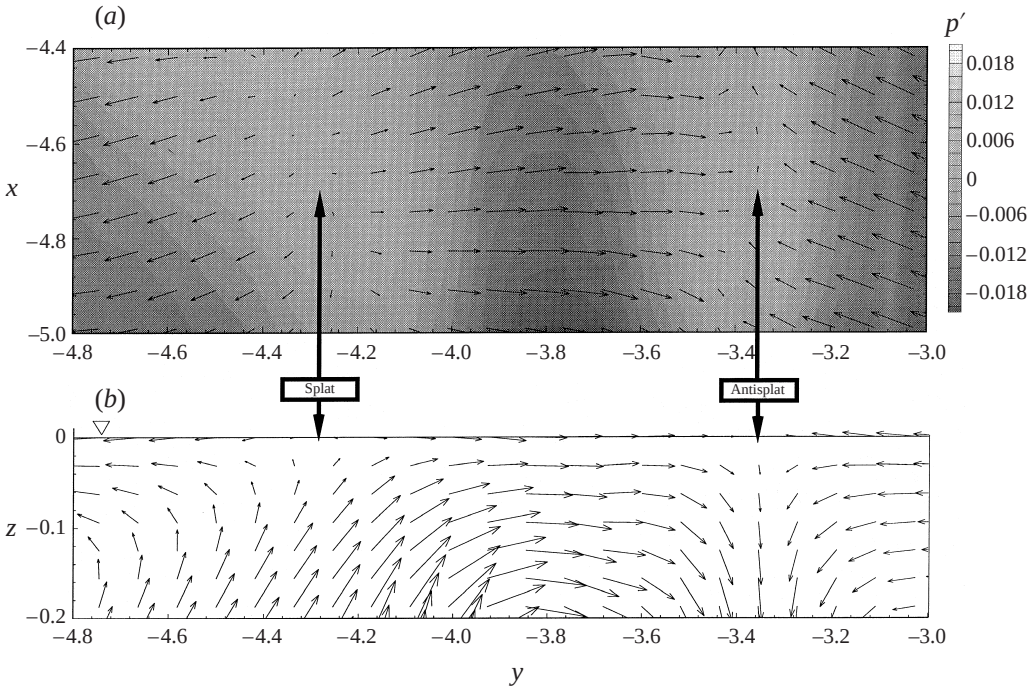

FIGURE 28. Splat and antisplat processes in FST. (*a*) Horizontal velocity vector (u', v') at the free surface. The background shows contours of the pressure fluctuation. (*b*) Velocity vector (v', w') in a vertical y, z section (at $x = -4.7$).

The transport term can be written as

$$-\frac{\partial}{\partial z}\overline{w'^3} - 2\frac{\partial}{\partial z}\overline{p'w'} = -\overline{3w'^2\frac{\partial w'}{\partial z}} - 2\overline{w'\frac{\partial p'}{\partial z}} - 2\overline{p'\frac{\partial w'}{\partial z}}. \tag{6.6}$$

The first two terms on the right are negligible for small Froude numbers while the third term cancels the pressure–strain correlation term. As a result, at the free surface, the transport term approximately balances the pressure–strain correlation term for small Froude numbers. (The balance is exact for zero Froude number.) We thus focus our attention on the pressure–strain correlation and perform a detailed analysis of the blockage effects of the free surface relative to a free-slip surface.

As fluid particles approach the free surface, they are forced to diverge and move in the horizontal directions. This is called the *splat* event. Based on the conservation of mass, the motion approaching the free surface must be balanced by the motion leaving the surface. The latter is called *antisplat* event. Splat and antisplat events are discussed by Perot & Moin (1995) for the zero Froude number case. Here we investigate the effects of the Froude number on these events.

The splat and antisplat events are manifested in the DNS results. Figure 28 shows a typical example. In a splat event (left side of figure 28), fluid moving towards the free surface turns near the surface and diverges horizontally. In an antisplat event (right side of figure 28), fluid particles moving towards each other at the surface meet and leave the surface. The centres of the splats and antisplats in figure 28(*a*) appear as respectively outward and inward nodal points of the velocity field in the (x, y)-plane and are therefore points of high pressure. In regions between splats and antisplats, horizontal velocities are high and the pressure is generally low (figure 28*a*).

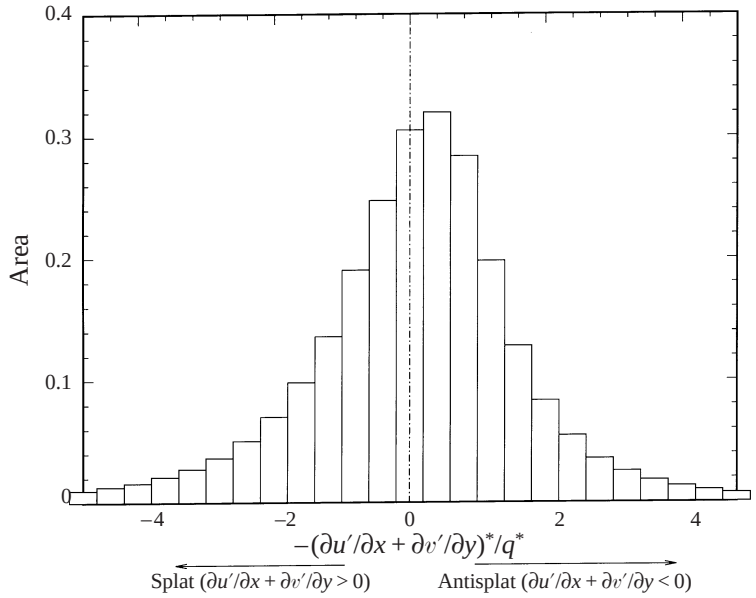

FIGURE 29. Area histogram based on the conditional average of splat and antisplat processes.

It should be pointed out that there exists another form of antisplat, which is the stretching of surface-connected vortices shown in § 4.3 (as well as another form of splat for the half-compression of surface-connected vortices at late evolution stages). Unlike that in figure 28, the antisplat occurring at a surface-connected vortex is characterized by high horizontal velocity and low pressure.

The splat event in figure 28 corresponds to the 'upwellings' described by Pan & Banerjee (1995) or the 'splat' model Leighton *et al.* (1991) use. The antisplat event in figure 28 corresponds to the 'downdraughts' of Pan & Banerjee (1995). The aforementioned surface-connected vortices are the same as the 'spin' model of Leighton *et al.* (1991). To understand the effects of Froude number on pressure–strain correlation, we focus on the first two since they are responsible for most of the differences due to Froude number in the inter-component energy transfer.

To investigate the statistics of splat and antisplat events over the free surface, we perform conditional averaging based on different stages of the splat and antisplat processes. The condition for such averaging is specified at each grid point on the free surface by the value of $-(\partial u'/\partial x + \partial v'/\partial y)^*/q^*$. Here the superscript * indicates that the quantity is normalized by its r.m.s. value. Positive/negative $\partial u'/\partial x + \partial v'/\partial y$ (negative/positive $\partial w'/\partial z$) corresponds to splats/antisplats respectively. This value, further divided by velocity fluctuation $q \equiv (u'^2 + v'^2 + w'^2)^{1/2}$, quantifies the splat and antisplat processes. Large values indicate that the fluid particle is close to the core of a splat/antisplat (large horizontal velocity divergence but small velocity at the stagnant points) while small values correspond to the neutral region between a splat and an antisplat (small divergence but large velocity when travelling along the surface).

Figure 29 shows the area histogram according to the above criterion. It is shown that most grid points at the free surface are located in the neutral region between splats and antisplats. It is also seen that the area of the antisplat region is larger than that of the splat region. (The ratio is about 55% to 45%.)

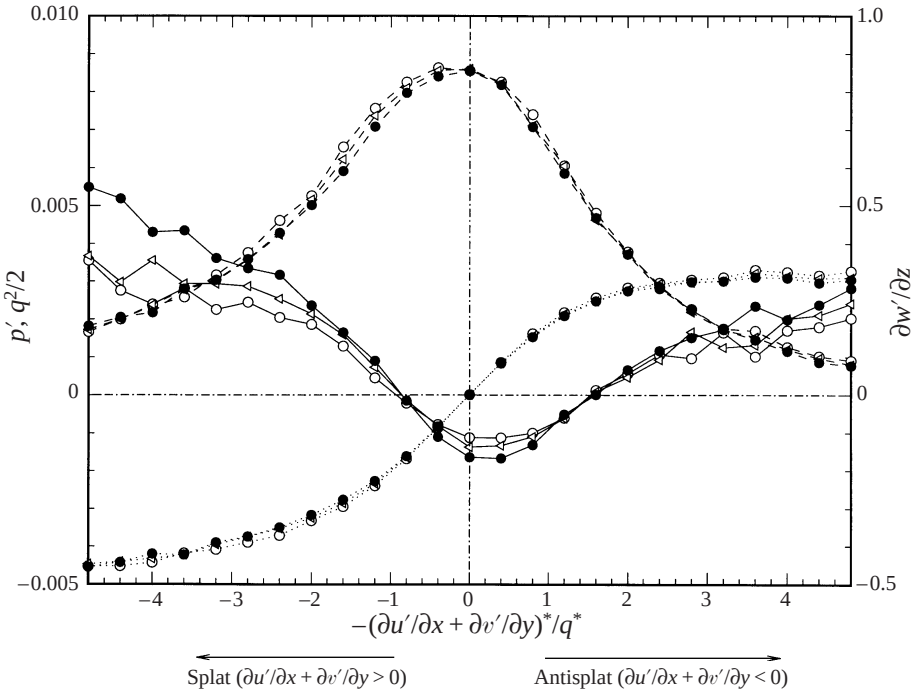

FIGURE 30. Conditional average of pressure fluctuation p', turbulence kinetic energy $q^2/2 = (u'^2 + v'^2 + w'^2)/2$, and $\partial w'/\partial z$ during splat and antisplat processes: ———, p'; – – – –, $q^2/2$; · · · · · · ·, $\partial w'/\partial z$. The symbol ○ refers to $Fr = 0.7$, ◁ to $Fr = 0.35$ and ● to $Fr = 0$.

Figure 30 shows the conditional average of turbulence kinetic energy and pressure fluctuation at each stage of splat/antisplat processes. At the free surface, following a fluid particle from splat to antisplat (from left to right in figure 28), the pressure is high at the splat while the kinetic energy is low there; in the middle between the splat and antisplat, the kinetic energy is high but the pressure is low; at the antisplat, the kinetic energy returns to a low value and the pressure increases again. This is consistent with figure 28.

It is important to point out that the curve of pressure fluctuation in figure 30 as well as the area histogram in figure 29 are not left–right symmetric; and the curve of $\partial w'/\partial z$ in figure 30 is not left–right anti-symmetric. Otherwise the overall integration of the pressure–strain correlation $\overline{p'\partial w'/\partial z}$ will be zero. It should also be mentioned that the region of surface-connected vortices is located near the central part in figure 30 since q is large for surface-connected vortices.

Figure 32 plots the histogram of pressure–strain correlation, which is the product of pressure fluctuation and $\partial w'/\partial z$ (figure 30) weighted by the area under figure 29. The histogram is not left–right anti-symmetric about the splat and antisplat. The integration gives the overall negative pressure–strain correlation at the free surface (figure 22), which indicates that the net energy transfer is from the vertical velocity component to horizontal components.

An important observation from figure 30 is that, although features like $(u'^2 + v'^2 + w'^2)/2$ and $\partial w'/\partial z$ do not depend very much on the Froude number, the pressure distribution during the splat and antisplat process is sensitive to the Froude number. It is shown that the pressure at splats and antisplats in the free-surface

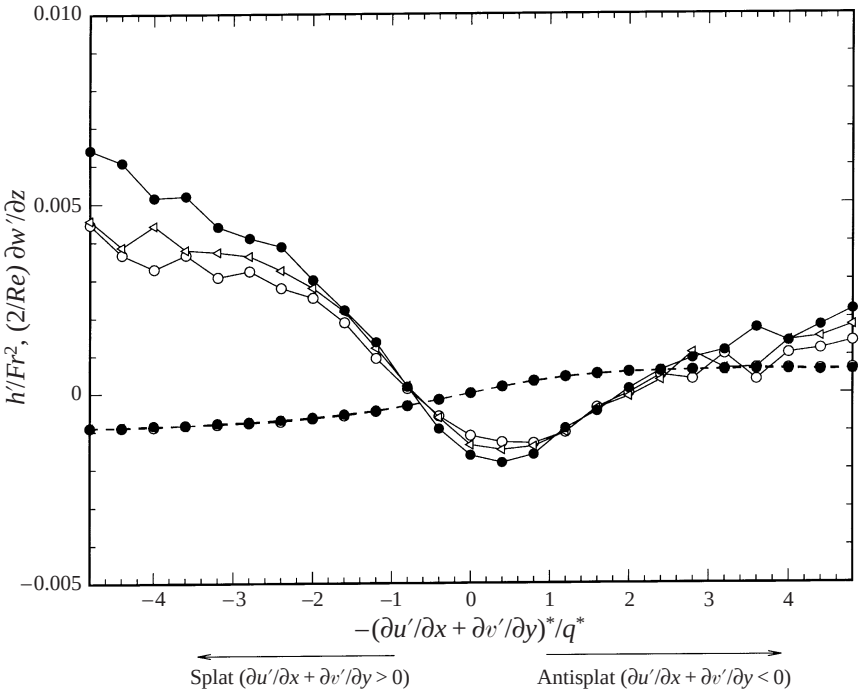

FIGURE 31. Conditional average of free-surface elevation h'/Fr^2 and viscous stress $(2/Re)\partial w'/\partial z$ during splat and antisplat processes: ———, h'/Fr^2; – – – –, $(2/Re)\partial w'/\partial z$. The symbol ○ refers to $Fr = 0.7$, ◁ to $Fr = 0.35$ and ● to $Fr = 0$. Here h'/Fr^2 is undefined for $Fr = 0$ where we plot the value $p' - (2/Re)\partial w'/\partial z$ instead.

case is considerably lower than that in the free-slip-plate case. The reduction of the pressure in the free-surface case shows that the deformable free surface relieves such impinging. Figure 30 also shows that due to the motions of the free surface, the pressure distribution at the free surface is smoother than that at the free-slip plate.

It should be noted that the reduction and the smoothing of the pressure during splats/antisplats at a deformable surface does not cause an obvious reduction in the global statistics of pressure fluctuation p'^{rms} (table 1). This issue is subtle: the deformable free surface only changes the *local distribution* of pressure in the splats/antisplats process. Therefore, only when we use the conditional averaging technique to highlight the distribution in the splats/antisplats process, does the difference caused by different Froude numbers appear as shown in figure 30.

The difference in the pressure distribution is caused by the distribution of free-surface elevation. The free-surface dynamic boundary condition (2.5) states that the pressure fluctuation p' at $z = 0$ is given by two parts: the hydrostatic pressure h'/Fr^2 and the viscous stress $(2/Re)\partial w'/\partial z$. Figure 31 plots the distribution of h'/Fr^2 and $(2/Re)\partial w'/\partial z$ during the splat and antisplat process. During a splat ($\partial w'/\partial z < 0$), p' is smaller than h'/Fr^2, while during an antisplat ($\partial w'/\partial z > 0$), p' is larger than h'/Fr^2. As figure 31 shows, the dependence of $(2/Re)\partial w'/\partial z$ on the Froude number is negligible. It is the hydrostatic pressure h'/Fr^2 that is sensitive to the Froude number. Note that, similar to the pressure distribution, the r.m.s. value of h'/Fr^2 for the whole (x, y)-plane does not differ much as the Froude number changes, i.e. h'^{rms} is scaled by Fr^2. It is the *local distribution* of h'/Fr^2 that is sensitive to the Froude number which is only shown using the conditional averaging in figure 31.

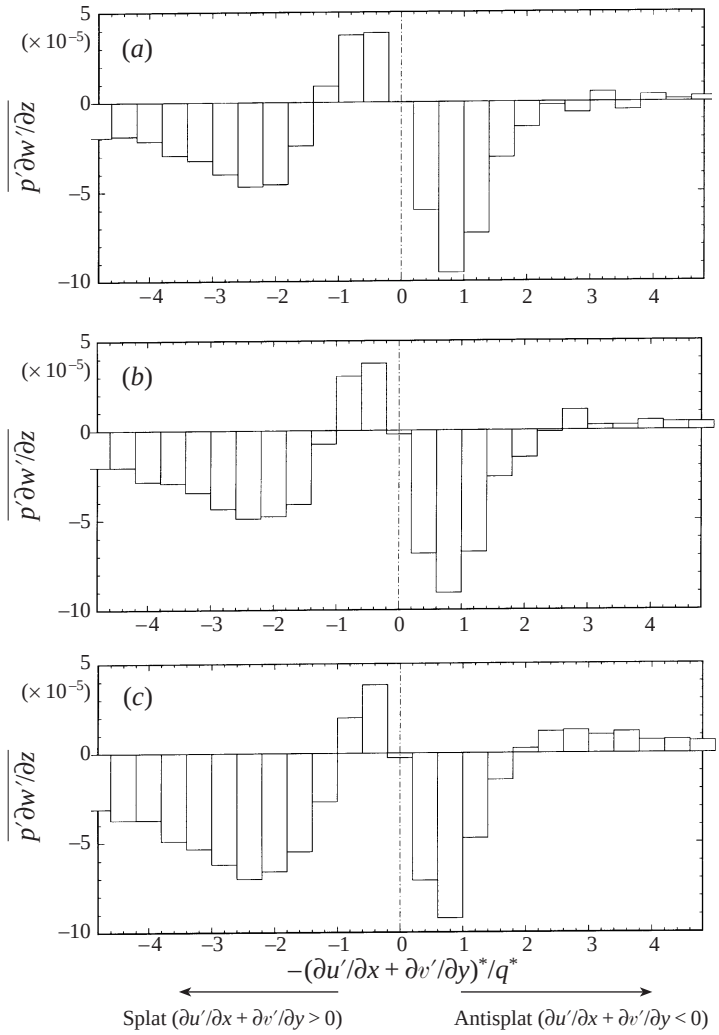

FIGURE 32. Histogram of pressure–strain correlation $\overline{p'\partial w'/\partial z}$ based on the conditional average of splat and antisplat processes: (*a*) $Fr = 0.7$; (*b*) $Fr = 0.35$; and (*c*) $Fr = 0$.

Since the pressure distribution over the splats/antisplats process depends on the Froude number, the pressure–strain correlation is directly affected. Figure 32(*a–c*) compares the histogram of $\overline{p'\partial w'/\partial z}$ among the $Fr = 0.7$, 0.35, and 0 cases. It is shown that the free surface transfers considerably less energy from the vertical velocity component to horizontal components than the free-slip-plate. As shown in figure 22, the effect of Froude number on the pressure–strain correlation is felt throughout the blockage layer.

In conclusion, it is shown that the local distribution of pressure (free-surface elevation) during the splats/antisplats process is sensitive to the Froude number. Accordingly, the pressure–strain correlation in free-surface turbulence is considerably less than that in free-slip-plate turbulence, even at low Froude numbers. Although the difference in pressure–strain correlation is partially balanced by the corresponding variations in the remaining terms in the Reynolds-stress equations (figures 20–22)

and the eventual influence on Reynolds stresses is small, as shown in table 1, the sensitivity of the pressure–strain correlation to the Froude number indicates the essentially different physics in the inter-component energy transfer for FST. This is important for the modelling of FST. Moreover, the Froude number effects on the pressure field are of fundamental importance for the generation of surface waves. The effects revealed here are of leading order and should still obtain (and be stronger) for higher Froude numbers where other mechanisms such as those associated with nonlinear free-surface effects are present.

7. Discussion and conclusions

In this paper we use DNS to study turbulent shear flow with a free surface at low Froude numbers. We identify a three-layer structure which is essential to understanding free-surface turbulence: the deeply submerged part of the flow, a blockage layer (thin compared to the vertical extent of the shear in the flow), and a much thinner surface layer immediately under the free surface. The blockage layer results from the kinematic boundary condition at the free surface, and the surface layer is caused by the dynamic zero-stress conditions.

The blockage layer is manifested in the vertical velocity fluctuations, which decrease to those imposed by the kinematic boundary condition at the surface. This reduction of the vertical velocity fluctuation occurs without any appreciable increase of kinetic energy dissipation, and is primarily compensated by an increase of the horizontal velocity fluctuations. This effect has been observed in different flows with a free surface (e.g. Handler *et al.* 1993; Pan & Banerjee 1995; Walker *et al.* 1996), and can therefore be considered as a generic feature of free-surface turbulence.

The surface layer is indicated by the sharp transition of the two horizontal vorticity components and the vertical derivative of the vertical vorticity component, which are reduced from their bulk (isotropic) values to those imposed by the zero-stress conditions at the free surface. As a result, the surface layer is a region of decreased kinetic energy dissipation and increased enstrophy dissipation. The latter increase is highly localized around vortex connection events. In fact once an attachment event is completed, the enstrophy dissipation is locally reduced, resulting in significantly slower decay of the attached vortex. Since attachment events occur on a continuous basis, the enstrophy dissipation averaged over the horizontal plane shows an increase inside the surface layer as a permanent and prominent feature.

The surface layer makes it possible for vorticity features at the free surface to differ substantially not only from those in the bulk but also from those inside the blockage layer. This result is important for practical applications when information from surface sensing is used to deduce characteristics of the underlying flow.

Finally, we identify the importance of non-zero Froude number on free-surface turbulence. We show that, even for very low Froude numbers, there is a finite reduction of the pressure–strain correlation at the free surface relative to that obtained using a free-slip flat plate as a model for the free surface. This is due to the free-surface elevation which can cause pressure variations comparable to turbulent pressure fluctuations. This should be taken into account in the modelling of free-surface turbulence when the details of the near-surface hydrodynamics are of interest (for example, in the spreading of surfactants).

This research was supported by the Office of Naval Research under the program management of Dr E. P. Rood.

REFERENCES

Balint, J.-L., Vukoslavcevic, P. & Wallace, J. M. 1988 The transport of enstrophy in a turbulent boundary layer. In *Near-Wall Turbulence, Zoran Zaric Memorial Conference* (ed. S. J. Kline & N. H. Afgan) Hemisphere, pp. 932–950.

Bernal, L. P. & Kwon, J. T. 1989 Vortex ring dynamics at a free surface. *Phys. Fluids* A **1**, 449–451.

Borue, V., Orszag, S. A. & Staroselsky, I. 1995 Interaction of surface waves with turbulence: direct numerical simulations of turbulent open-channel flow. *J. Fluid Mech.* **286**, 1–23.

Bradshaw, P. & Koh, Y. M. 1981 A note on Poisson's equation for pressure in a turbulent flow. *Phys. Fluids* **24**, 777.

Dimas, A. A. & Triantafyllou, G. S. 1994 Nonlinear interaction of shear flow with a free surface. *J. Fluid Mech.* **260**, 211–246.

Gharib, M., Dabiri, D. & Zhang, X. 1994 Interaction of small scale turbulence with a free surface. In *Free-Surface Turbulence* (ed. E. P. Rood & J. Katz), pp. 97–102. ASME.

Handler, R. A., Swean, T. F. Jr., Leighton, R. I. & Swearingen, J. D. 1991 Length scales of turbulence near a free surface. *AIAA Paper* 91-1775.

Handler, R. A., Swean, T. F. Jr., Leighton, R. I. & Swearingen, J. D. 1993 Length scales and the energy balance for turbulence near a free surface. *AIAA J.* **31**, 1998–2007.

Harlow, F. H. & Welch, J. E. 1965 Numerical calculation of time-dependent viscous incompressible flow of fluid with free surface. *Phys. Fluids* **8**, 2182–2189.

Hinze, J. O. 1975 *Turbulence*. McGraw-Hill.

Hunt, J. C. R. & Graham, J. M. R. 1978 Free-stream turbulence near plane boundaries. *J. Fluid Mech.* **84**, 209–235.

Komori, S., Nagaosa, N., Murakami, Y., Chiba, S., Ishii, K. & Kuwahara, K. 1993 Direct numerical simulation of three-dimensional open-channel flow with zero-shear gas-liquid interface. *Phys. Fluids* A **5**, 115–125.

Kwak, D., Reynolds, W. C. & Ferziger, J. H. 1975 Three-dimensional, time-dependent computation of turbulent flow. *Rep.* TF-5 Mech. Engng Dept., Stanford University.

Lam, K. & Banerjee, S. 1988 Investigation of turbulent flow bounded by a wall and a free surface. In *Fundamentals of Gas-Liquid Flows* (ed. E. Michaelides & M. P. Sharma), pp. 29–38. ASME.

Leighton, R. I., Swean, T. F. & Handler, R. A. 1991 Interaction of vorticity with a free surface in turbulent open channel flow. *AIAA Paper* 91-0236.

Mattingly, G. E. & Criminale, W. O. 1972 The stability of an incompressible two-dimensional wake. *J. Fluid Mech.* **51**, 233–272.

Moin, P. & Kim, J. 1985 The structure of the vorticity field in turbulent channel flow. Part 1. Analysis of instantaneous fields and statistical correlations. *J. Fluid Mech.* **155**, 441–464.

Ohring, S. & Lugt, H. J. 1996 Interaction of an obliquely rising vortex ring with a free surface in a viscous fluid. *Meccanica* **31**, 623–655.

Pan, Y. & Banerjee, S. 1995 A numerical study of free-surface turbulence in channel flow. *Phys. Fluids* **7**, 1649–1664.

Perot, B. & Moin, P. 1995 Shear-free turbulent boundary layers. Part 1. Physical insights into near-wall turbulence. *J. Fluid Mech.* **295**, 199–227.

Rashidi, M. 1997 Burst-interface interactions in free surface turbulent flows. *Phys. Fluids* **9**, 3485–3501.

Sarpkaya, T. 1996 Vorticity, free surface, and surfactants. *Ann. Rev. Fluid. Mech.* **28**, 83–128.

Swean, T. F., Jr., Leighton, R. I., Handler, R. A. & Swearingen, J. D. 1991 Turbulence modeling near the free surface in open cannel flow. *AIAA Paper* 91-0613.

Tennekes, H. & Lumley, J. L. 1972 *A First Course in Turbulence*. The MIT Press.

Triantafyllou, G. S. & Dimas, A. A. 1989 Interaction of two-dimensional separated flows with a free surface at low Froude numbers. *Phys. Fluids* A **1**, 1813–1821.

Tsai, W. T. 1998 A numerical study of the evolution and structure of a turbulent shear layer under a free surface. *J. Fluid Mech.* **354**, 239–276.

Walker, D. T., Leighton, R. I. & Garza-Rios, L. O. 1996 Shear-free turbulence near a flat free surface. *J. Fluid Mech.* **320**, 19–51.

Zhang, C., Shen, L. & Yue, D. K. P. 1999 The mechanism of vortex connection at a free surface. *J. Fluid Mech.* **384**, 207–241.